arXiv:2506.14552v4 [hep-ph] 27 May 2026

Toponia at the HL-LHC and FCC-ee

Yang Bai[a,b], Ting-Kuo Chen[a], and Yiming Yang[a]

[a] *Department of Physics, University of Wisconsin-Madison, Madison, WI 53706, USA*
[b] *HEP Division, Argonne National Laboratory, Argonne, IL 60439, USA*

Abstract

The hint of a pseudoscalar toponium state at the Large Hadron Collider (LHC) opens a new avenue for studying a novel class of QCD (quasi-)bound states with comparable formation and decay times. Compared with charmonium and bottomonium, toponium is a quasi-bound state, resembling a hydrogen atom of the strong interaction, although it appears as a broader resonance. We compute the masses and annihilation decay widths of the lowest S-wave (η_t, ψ_t) and P-wave (χ_{t0}, χ_{t1}) toponium states, and assess their discovery prospects at the High-Luminosity LHC (HL-LHC) and future lepton colliders, such as the e^+e^- stage of the Future Circular Collider (FCC-ee). Detecting the vector ψ_t state at the HL-LHC is hindered by the Landau–Yang theorem and the gluon-dominated production environment of the collider, whereas lepton colliders offer promising sensitivity through both constituent and two-body decays. A more precise measurement of the η_t mass—approximately equal to that of ψ_t—at the LHC could help determine the optimal $t\bar{t}$ threshold center-of-mass energy for FCC-ee. The P-wave states remain challenging to observe at both the HL-LHC and future lepton colliders. We also discuss how toponium measurements can be used to probe top-quark properties and to conduct indirect searches for new physics, including light scalars that couple to the top quark.

Contents

1 Introduction **2**

2 Properties of toponium states **4**
2.1 Mass spectrum 4
2.2 Decays 7
2.3 Production 8

3 Sensitivity of toponium states at the LHC and future colliders **12**
3.1 η_t 12
3.2 ψ_t 17
3.3 χ_t 22

4 Toponium as a probe for the real singlet extension **23**

5 Discussion and conclusions **25**

A Partial width formulas for the annihilation decay modes **27**

B Green function method for P-wave states **31**

1 Introduction

Toponium, the quasi-bound state [1] formed by a top quark t and an anti-top quark $\bar{t}$, is the smallest bound state known to date in the Standard Model (SM). Characterized by a Bohr radius of $\sim 0.01\,\text{fm}$, the properties of toponia are predominantly captured by perturbative Quantum Chromodynamics (pQCD) in the short-distance regime, hence providing a novel probe for QCD properties including its asymptotic freedom behavior. Moreover, as the threshold production of $t\bar{t}$ at lepton colliders provides an efficient way to measure the properties of the top quark, such as its mass m_t and decay width Γ_t [2], the study of the quasi-bound-state effects of toponia is crucial for the complete understanding of the SM.

The quest for toponium at colliders has long been discussed in the literature, both at hadron colliders [3–14] and lepton colliders [15–41] (some more general studies on toponium phenomenology can be found in Refs. [42–44]). From the theoretical perspective, it is also important to fully understand the QCD potential between the constituent t and $\bar{t}$ to precisely predict the properties of toponia, which has long been an active field of research until now [42, 45–50]. Without loss of generality, there are three main methodological categories for the phenomenological predictions near the $t\bar{t}$ threshold: 1. quantum-mechanical-like spectroscopy calculated with the wavefunction projection method (for both production cross sections and decays) [3, 4, 43, 46, 49, 50], 2. the Green-function method which takes the large-width effect of top quarks into account [5–7, 13, 16, 18–21, 25, 28], and 3. effective field theories that provide more systematic controls over theoretical uncertainties [8, 10, 11, 23, 24, 27, 29–31, 34–37, 39, 40, 51, 52]. We note here that these methods are not necessarily mutually exclusive and can be combined. Furthermore, the $t\bar{t}$ "resonance" can offer insights into potential new physics, such as that the resonance actually comprises a pseudoscalar state of a mass around $2m_t$ [53, 54] or that there are exotic short-range interactions "nailing" t and $\bar{t}$ together on top of the gluonic force [55]. Besides high energy physics, the resonance production near the $t\bar{t}$ threshold also offers a wonderful playground for the exploration of quantum mechanical properties of particles, including polarizations, spin correlations, entanglement, and the testing of Bell non-locality [56–61].

Recently, both CMS and ATLAS have reported the cross-section enhancement near the $t\bar{t}$ production threshold in the pseudoscalar channel at the Large Hadron Collider (LHC) with a significance of over $5\,\sigma$ [62, 63]. This enhancement could receive a sizable contribution from the pseudoscalar toponium state η_t. However, the Coulomb-enhanced continuum slightly above the threshold may also contribute significantly (see Table 6 of Ref. [51]), given the relatively large bin size of the $t\bar{t}$ invariant mass used in experimental searches. Fixing the top quark Monte Carlo mass $m_t^{\text{MC}} = 172.5$ GeV and $M_{\eta_t} = 343$ GeV (which implies a binding energy of $E_{\text{bind}} = M_{\eta_t} - 2m_t^{\text{MC}} = -2$ GeV) in the Monte Carlo simulation, the production cross section is measured to be $\sigma(pp \to \eta_t) = 8.8^{+1.2}_{-1.4}$ pb by CMS and $9.3^{+1.4}_{-1.3}$ pb by ATLAS. This opens an avenue for the study of a novel class of QCD (quasi-)bound states with a bound state formation time of $\mathcal{O}[(\alpha_s^2 m_t)^{-1}]$ that is comparable to their decay time of $(2\Gamma_t)^{-1}$. Because of the large

[1] The binding energy of toponium, or equivalently the inverse of the bound-state formation time, is comparable to the decay width of the constituent top and anti-top quarks. As a result, the two-body system barely completes even a single round of orbital motion before the constituents decay. In this sense, the term "quasi-bound state" may be more appropriate, although throughout this paper we will use "toponium" and "quasi-bound state" interchangeably. This behavior is related to the fact that the corresponding pole of the scattering amplitude lies relatively far from the real axis on the second Riemann sheet of the complex energy plane [1].

top quark decay width, the toponium states behave as relatively broader resonances compared to the charmonium and bottomonium states. Furthermore, the leading discovery channel of toponium states relies on the leading constituent decay channel and not on the suppressed (with branching ratios of less than 10^{-3}) annihilation decay channels, which is opposite to the charmonium/bottomonium system.

Because of their small relative velocity, the binding force between the constituent t and $\bar{t}$ within a toponium system at the production threshold can be well described by the static QCD potential [64–67], with which one can solve the corresponding non-relativistic Schrödinger equation to obtain several properties of the toponium, such as its binding energy (and thus total bound-state mass) and wavefunction. Due to the large top quark decay width $\Gamma_t = 1.42$ GeV [68], the dominant decay mode of a toponium is its intrinsic decay via the decays of individual constituents t and $\bar{t}$. Nevertheless, as we will discuss more in Section 3, some $t\bar{t}$-annihilation decay modes of a toponium can provide additional probes for other SM properties such as the top Yukawa coupling [69, 70]. To study these decays, one can use the projection method [42, 71] to isolate the partial-wave toponium state of interest, which can also be used to study the production of toponia at colliders. However, since the projection method does not take into account the interplay between the continuous $t\bar{t}$ and bound-state toponium production mechanisms, certain quantities (such as the differential cross section $\mathrm{d}\sigma/\mathrm{d}m_{t\bar{t}}$, $m_{t\bar{t}}$ being the invariant mass of the $t\bar{t}$ system) must be computed using other methods. For example, the Green function method [6–8, 15, 16, 29, 72] makes use of the optical theorem to incorporate bound-state effects into the continuous spectrum, although how these two effects should be distinguished is still a topic under active research, as we will explain more in Section 2. Nevertheless, as we show later, these two methods give comparable $pp \to \eta_t$ cross sections around and below the threshold that are also consistent with the CMS [62] and ATLAS [63] measurements, which allows the use of the projection method for our purpose of surveying the sensitivity of several toponium states at the current LHC and other future colliders.

As mentioned earlier, since the study of toponia is crucial for the complete understanding of the SM, it is of great importance to survey other possible search channels than the $pp \to \eta_t \to bW^+\bar{b}W^-$ process at the current LHC. For example, in this study, we find that the $\eta_t b\bar{b}$ production can be sensitive at the High-Luminosity LHC (HL-LHC). On the other hand, although it is difficult for η_t to be directly produced at lepton colliders due to its J^{PC} quantum numbers, ψ_t turns out to be a fairly promising state to be probed at these facilities, which has been pointed out for long in the literature (see for example Refs. [18, 20, 27, 29]). On the contrary, the direct production of $gg \to \psi_t$ is prohibited by the Landau-Yang theorem [73, 74], and thus it is challenging to discover ψ_t at hadron colliders. In this study, we especially discuss the e^+e^- stage of the Future Circular Collider (FCC-ee) [75–77], the preferred option for CERN suggested by the European Strategy Group [78], which proposes to run around the $t\bar{t}$ threshold with an integrated luminosity of $\mathcal{O}(1)$ ab^{-1}. For ψ_t, in addition to the individual t and $\bar{t}$ decays, Ref. [40] shows that its leading $t\bar{t}$-annihilation decay to $b\bar{b}$ can also be probed via some specially designed observable that captures the interference with the γ- and Z-mediated processes caused by the ψ_t mass pole. In this study, we independently calculate the production cross section including the interference effects and identify a sign mistake in Ref. [52] (their earlier work Ref. [40] and the public model file are both correct), which leads to a larger cross section in their result compared to the correct numbers presented in this study. Moreover, one can also perform sensitive studies

on other promising channels, such as processes $e^+e^- \to \psi_t \to W^+W^-, \gamma Z,$ and γH.

Finally, in addition to probing the SM, one can also constrain certain beyond-SM (BSM) physics with toponium measurements, such as new scalar fields that either affect the top Yukawa coupling of the 125-GeV Higgs boson or contribute additional Yukawa interactions to the static toponium QCD potential. In our study, we use the $\mathbb{Z}_2$-symmetric real-singlet extension to the SM (SSM) as an example and show how the η_t measurement performed in Ref. [62] can be used to constrain its parameter space, while one can certainly generalize this idea to other BSM models.

Our paper is organized as follows. In Section 2, we review the theoretical properties of toponia, including their masses, decays, and production at colliders, with the details of the $t\bar{t}$-annihilation decay formulas and the results of P-wave Green function calculation summarized in Appendices A and B, respectively. In Section 3, we discuss the discovery sensitivity of the four toponium states η_t, ψ_t, χ_{t0}, and χ_{t1} at the current LHC and future HL-LHC and FCC-ee. In Section 4, we perform a parameter space study on the SSM using the η_t measurement conducted by CMS as an example of probing BSM physics using toponium. Finally, we conclude our study in Section 5.

2 Properties of toponium states

In this section, we summarize some basic properties of the toponium states, including their mass spectrum, decays, and production at colliders.

2.1 Mass spectrum

The binding energy and wavefunction of a heavy quarkonium near the threshold can be obtained by solving the non-relativistic Schrödinger equation given the small velocities of the constituent quarks. For a color-singlet toponium system in the short-distance regime, the associated static potential described by pQCD up to two-loop is given by [8, 64–68]

$$V_{\rm pQCD}(r) = -\frac{C_F\,\alpha_s(\mu_R)}{r}\left\{1+\frac{\alpha_s(\mu_R)}{4\pi}[a_1+2\gamma_E\beta_0] + \left(\frac{\alpha_s(\mu_R)}{4\pi}\right)^2\left[a_2+\left(\frac{\pi^2}{3}+4\gamma_E^2\right)\beta_0^2+2\gamma_E(2a_1\beta_0+\beta_1)\right]\right\}\,, \tag{2.1}$$

where $\gamma_E \approx 0.577$ is the Euler-Mascheroni constant and $\alpha_s(\mu_R)$ is the strong coupling at the renormalization scale μ_R as given by

$$\alpha_s(\mu_R) = \frac{4\pi}{\beta_0\log(\mu_R^2/\Lambda^2)}\left\{1-\frac{\beta_1}{\beta_0^2}\frac{\log\left[\log(\mu_R^2/\Lambda^2)\right]}{\log(\mu_R^2/\Lambda^2)}\right\}\,. \tag{2.2}$$

A convenient scale choice of μ_R is $\sim 1/r$, which we will stick to in this study and check the related variation later. The color $SU(3)$ group constants are defined through $C_F = 4/3$, $C_A = 3$, $T_F = 1/2$, $n_f = 5$, $\beta_0 = 11C_A/3 - 4T_Fn_f/3$, $\beta_1 = 34C_A^2/3 - 20C_AT_Fn_f/3 - 4C_FT_Fn_f$, and

$$a_1 = \frac{31}{9}C_A - \frac{20}{9}T_Fn_f\,, \tag{2.3}$$

$$a_2 = \left[\frac{4343}{162} + 4\pi^2 - \frac{\pi^4}{4} + \frac{22}{3}\zeta(3)\right] C_A^2 - \left[\frac{1798}{81} + \frac{56}{3}\zeta(3)\right] C_A T_F n_f$$
$$- \left[\frac{55}{3} - 16\zeta(3)\right] C_F T_F n_f + \left[\frac{20}{9} T_F n_f\right]^2 . \tag{2.4}$$

In the long-distance regime, one can replace the potential in Eq. (2.1) with the Cornell potential

$$V_{\text{Cornell}} = -\frac{C_F\, \alpha_s^{\text{Cornell}}}{r} + b\, r \ , \tag{2.5}$$

starting from the transition point $r = r_0 = 0.1$ fm, where $\alpha_s^{\text{Cornell}} = 0.211$ and $b = 0.212$ GeV^2 are taken to be fixed values evaluated at the transition point (see Ref. [79] for the results from Lattice QCD calculations). Overall, one has the complete static potential

$$V_{\text{static}}(r) = \begin{cases} V_{\text{pQCD}}(r) & , \quad r \leq r_0 \\ V_{\text{Cornell}}(r) & , \quad r > r_0 \end{cases} . \tag{2.6}$$

Note that the Bohr radius of the toponium states a_t can be estimated using the Coulomb potential as $a_t = (C_F\, \alpha_s\, m_t/2)^{-1} \sim (18 \text{ GeV})^{-1}$. One then has $\alpha_s = \alpha_s(a_t^{-1}) \approx \alpha_s(18 \text{ GeV}) \approx 0.157$ and $a_t \approx 0.011$ fm [68], which is one order of magnitude smaller than the transition radius r_0. This also means that the properties of toponia are dominated by the short-distance pQCD potential.

To calculate the mass splitting among the different toponium states with the same orbital angular momentum, one can use the spin-dependent potential [80]

$$V_{\text{spin-dep}}(r) = \frac{8\, \alpha_s(\mu_R)}{9\, m_t^2\, r^2} \delta(r)\, \vec{\text{S}}_t \cdot \vec{\text{S}}_{\bar{t}} + \frac{1}{m_t^2} \left[\left(\frac{2\alpha_s(\mu_R)}{r^3} - \frac{b}{2r} \right) \vec{\text{L}} \cdot \vec{\text{S}} + \frac{4\alpha_s(\mu_R)}{r^3} \text{T} \right] . \tag{2.7}$$

Here, $\vec{\text{S}}_t$ and $\vec{\text{S}}_{\bar{t}}$ are the spin operators of the top and anti-top quarks, respectively. $\vec{\text{S}} = \vec{\text{S}}_t + \vec{\text{S}}_{\bar{t}}$ is the total spin angular momentum operator, $\vec{\text{L}}$ is the orbital angular momentum operator, and $\vec{\text{J}} = \vec{\text{S}} + \vec{\text{L}}$ is the total angular momentum operator. We denote S, L, J as the eigenvalues of the corresponding angular momentum operators. The tensor operator T has non-zero eigenvalues only between the $L > 0$ spin-triplet states as

$$\langle {}^3L_J | \, \text{T} \, | {}^3L_J \rangle = \begin{cases} -\frac{L}{6(2L+3)} & , \quad J = L+1 \\ +\frac{1}{6} & , \quad J = L \\ -\frac{L+1}{6(2L-1)} & , \quad J = L-1 \end{cases} . \tag{2.8}$$

By solving the Schrödinger equation with the full static potential given in Eq. (2.6), one can obtain the binding energy E_{bind} (which can be either positive or negative) and wavefunction of a given toponium state. The bound-state mass of a toponium is then given by $M = 2\, m_t + E_{\text{bind}}$, where the top quark mass is taken to be the measured pole mass $m_t = m_t^{\text{pole}} = 172.4 \pm 0.7$ GeV [68]. The uncertainty in m_t will introduce an uncertainty in the toponium mass of around $\delta M \approx 1.4$ GeV. Moreover, since there is no definitive way to fix μ_R, the range of this

toponium	binding energy [GeV]		$R_S(0)$ $[a_t^{-3/2}]$, $R'_P(0)$ $[a_t^{-5/2}]$	
	$m_t = 172.4 \pm 0.7$ GeV	$\mu_R = (1.0^{+1.0}_{-0.5})/r$	m_t	μ_R
S-wave	$-2.725^{+0.005}_{-0.005}$	$-2.725^{+0.654}_{-1.020}$	$1.611^{+0.001}_{-0.001}$	$1.611^{+0.235}_{-0.205}$
P-wave	$-1.375^{+0.003}_{-0.003}$	$-1.375^{+0.430}_{-0.813}$	$0.2346^{+0.0003}_{-0.0003}$	$0.2346^{+0.0208}_{-0.0444}$

Table 1: The binding energies and (derivatives of) the radial wavefunctions at the origin for the lowest S-wave and P-wave toponium states obtained by solving the Schrödinger equation with the full $V_{\text{static}}(r)$ given in Eq. (2.6). The Bohr radius is $a_t = [C_F\, \alpha_s(a_t^{-1})\, m_t/2]^{-1}$. The uncertainties come either from the experimental uncertainty in m_t or the variation of the renormalization scale μ_R from $0.5/r$ to $2/r$.

choice will lead to an additional uncertainty of $\mathcal{O}(1\,\text{GeV})$ in δM through $\alpha_s(\mu_R)$, which can be seen in Table 1, in which we investigated the binding energies and the values at the origin of the wavefunctions $R_S(r)$ [the derivatives of wavefunctions $R'_P(r)$] for the S-wave (P-wave) states, respectively, by varying μ_R from $0.5/r$ to $2/r$. Overall, the uncertainty in the predicted toponium mass is $\delta M \simeq 2$ GeV. Using the obtained wavefunctions and Eq. (2.7), we calculate the mass splittings among the states with the same L and show the spectrum of the first few S- and P-wave states in Figure 1, where we fix the top quark mass m_t at its central value 172.4 GeV and the renormalization scale $\mu_R = 1/r$. Note that all toponia have an uncertainty of around $\delta M \sim 2$ GeV coming from the uncertainties in m_t and μ_R as mentioned previously, while the relative mass differences are all much smaller and thus negligible.

Note that because $\alpha_s(a_t^{-1})/\pi \approx 0.05 \ll 1$ for a typical toponium system, it can be well described by pQCD through the leading-order Coulomb potential $V_{\text{Coul}}(r) = -C_F \alpha_s^{\text{Coul}}/r$, where α_s^{Coul} is a fixed number whose value we will determine later, with both the loop correction and linear potential neglected. Likewise, the other S, L, J, T-dependent terms are subdominant compared to V_{Coul} and will only produce small splittings among the masses of the different toponium states, which we label using the term symbol ${}^{2S+1}L_J$. As a result, as far as the wavefunctions of the different toponium states are concerned, taking $V \approx V_{\text{Coul}}$ is in general a good approximation. To demonstrate this, we fix α_s^{Coul} by matching the derived binding energy of the S-wave states to that calculated from using the full $V_{\text{static}}(r)$ given in Eq. (2.6). This matching leads to $\alpha_s^{\text{Coul}} = 0.189$. We then compare the values of the radial wavefunctions of the two lowest S-wave states $\eta_t({}^1S_0), \psi_t({}^3S_1)$ $[R_S(r)]$ and the derivatives of those of the two lowest P-wave states $\chi_{t0}({}^3P_0), \chi_{t1}({}^3P_1)$ $[R'_P(r)]$ at the origin $r = 0$ using both $V_{\text{Coul}}(r)$ and the full $V_{\text{static}}(r)$. We list the latter in Table 1, while the former are given by

$$R_S(0) = 2\left(\frac{4}{3}\frac{\alpha_s^{\text{Coul}} m_t}{2}\right)^{\frac{3}{2}} = 2(a_t^{\text{Coul}})^{-\frac{3}{2}}, \quad R'_P(0) = \frac{1}{\sqrt{24}}\left(\frac{4}{3}\frac{\alpha_s^{\text{Coul}} m_t}{2}\right)^{\frac{5}{2}} \approx 0.2041(a_t^{\text{Coul}})^{-\frac{5}{2}}\,, \tag{2.9}$$

with the binding energies of the P-wave states being -0.6812 GeV. One can see that the two methods indeed give close though not identical results. This discrepancy can be explained by the following reasons. First, when $r \to 0$, the full potential V_{static} will be suppressed through the running of $\alpha_s(\mu_R \sim 1/r)$ due to the asymptotic freedom of QCD, while V_{Coul} remains

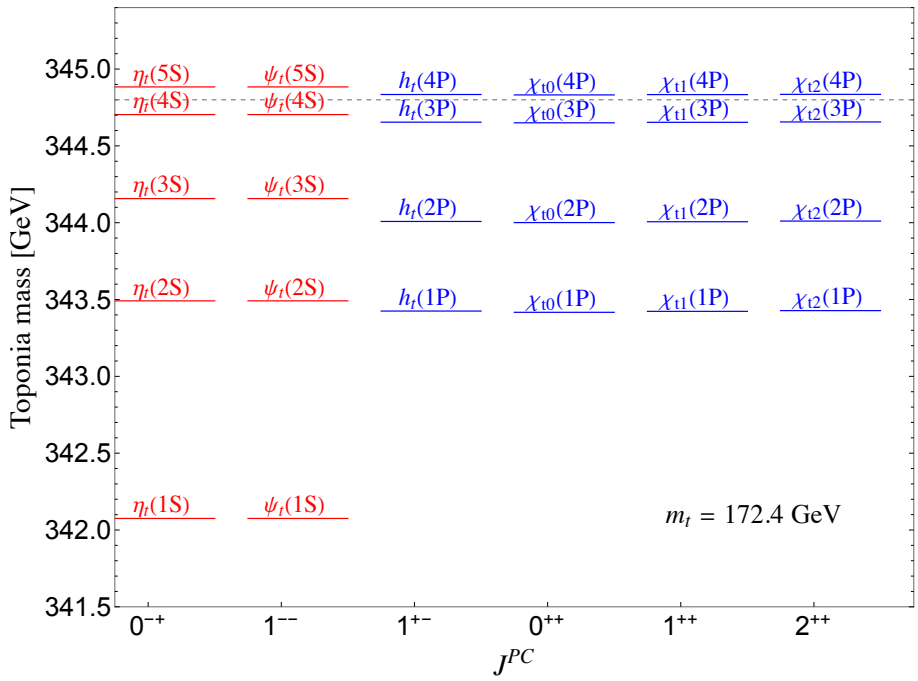

Figure 1: The mass spectrum of the lowest S- and P-wave toponium states, categorized by their principal quantum number n and $n-1$ and $J^{\rm PC}$ quantum numbers. In this plot, we fix $m_t = 172.4$ GeV, and the gray dashed line denotes the threshold mass $2m_t = 344.8$ GeV, above and below which $E_{\rm bind} > 0$ and $E_{\rm bind} < 0$, respectively. The renormalization scale for $\alpha_s(\mu_R)$ in the static potential is chosen to be $\mu_R = 1/r$. There is an uncertainty of around $\delta M \sim 2$ GeV for all toponium masses resulting from the top quark mass and renormalization scale uncertainties. The mass difference between $\eta_t(n{\rm S})$ and $\psi_t(n{\rm S})$ is negligible and that among the P-wave states with the same principle quantum number $n-1$ is around 5 MeV. On the other hand, the mass splitting between S- and P-wave states with the same principle quantum number n is sizable, *e.g.*, the mass difference between $\eta_t(2S)$ and $h_t(1P)$ is 66 MeV.

parametrized by the fixed $\alpha_s^{\rm Coul}$. This difference between the behavior of the two potentials at short distance will then influence (the derivatives of) the wavefunctions at the origin. Second, the P-wave wavefunctions are distributed considerably about $r \sim \mathcal{O}(1)a_t$, which causes them to receive more corrections from the long-distance contribution of the static potential compared to the S-wave states. We further scan $\kappa \equiv \mu_R \times r$ and find that the larger κ, the more similar the S-wave wavefunctions derived with $V_{\rm static}$ and $V_{\rm Coul}$ will be. This is because $\alpha_s(\mu_R = \kappa/r)$ will decrease along with shorter r, making the system more similar to the case described only by $V_{\rm Coul}$, which after matching $E_{\rm bind} = -1.88$ GeV is parametrized by $\alpha_s = \alpha_s(a_t^{-1}) = 0.157$. In the remainder of the study, we will only use $V_{\rm Coul}$ with $\alpha_s^{\rm Coul} = 0.189$ to calculate the wavefunctions for simplification, which we will discuss more in Section 3.1.

2.2 Decays

The dominant decay mode of toponia is the intrinsic decays of the constituent top and anti-top quarks with the decay width $\Gamma \approx \Gamma_t + \Gamma_{\bar{t}} = 2\Gamma_t = 2.84$ GeV [68]. On top of that, one can

also consider the $t\bar{t}$-annihilation decay modes, which have been considered in Refs. [42, 71] and calculated using the "projection method", which works as follows: Consider a generic $Q\bar{Q} \to f$ annihilation process with the matrix element

$$\mathcal{M}(Q\bar{Q} \to f) = \bar{v}^s \left(\frac{p}{2} - q\right) \mathcal{O}(p,q) u^{s'} \left(\frac{p}{2} + q\right) \ , \tag{2.10}$$

from which we further define $\mathcal{O}(0) \equiv \mathcal{O}(p, q = 0)$ and $\mathcal{O}^\alpha(0) \equiv \frac{\partial}{\partial q_\alpha}\mathcal{O}(p,q)|_{q=0}$. Consequently, one can write down the bound-state version of the matrix element $\mathcal{M}[B(^{2S+1}L_J) \to f] \equiv \mathcal{A}(^{2S+1}L_J)$ in the non-relativistic limit, where $B(^{2S+1}L_J)$ is the $Q\bar{Q}$ bound state characterized by the quantum numbers S, L, J. For the S-wave states, one has

$$\mathcal{A}(^1S_0) = \frac{1}{\sqrt{3}}\frac{1}{\sqrt{M_B}}\frac{1}{2}\frac{1}{\sqrt{4\pi}} R_S(0)\, \mathrm{Tr}\big[\mathcal{O}(0)(M_B + \not{p})(-\gamma^5)\big] \ , \tag{2.11}$$

$$\mathcal{A}(^3S_1) = \frac{1}{\sqrt{3}}\frac{1}{\sqrt{M_B}}\frac{1}{2}\frac{1}{\sqrt{4\pi}} R_S(0)\, \mathrm{Tr}[\mathcal{O}(0)(M_B + \not{p})(-\gamma^\mu)]\varepsilon_\mu(p) \ , \tag{2.12}$$

where $\varepsilon_\mu(p)$ is the polarization vector of the $^3S_1$ state, which is the ψ_t state when it comes to toponium. Note that the trace is also taken over the color indices, while the prefactor $\frac{1}{\sqrt{3}}$ arises from the projection onto the color-singlet component of the $Q\bar{Q}$ bound state. As for the P-wave states, one has

$$\mathcal{A}(^1P_1) = \frac{1}{\sqrt{3}}\frac{i}{\sqrt{M_B}}\frac{1}{2}\sqrt{\frac{3}{4\pi}} R_P'(0)\, \mathrm{Tr}\left[\left[\mathcal{O}^\mu(0) - \frac{2}{M_B}\mathcal{O}(0)\gamma^\mu\right](M_B + \not{p})\gamma^5\right]\varepsilon_\mu(p) \ , \tag{2.13}$$

$$\mathcal{A}(^3P_0) = \frac{1}{\sqrt{3}}\frac{i}{\sqrt{M_B}}\sqrt{\frac{1}{4\pi}} R_P'(0)\, \mathrm{Tr}\left[\frac{1}{2}\mathcal{O}^\mu(0)(\gamma_\mu + \frac{p_\mu}{M_B})(\not{p} - M_B) + 3\mathcal{O}(0)\right] \ , \tag{2.14}$$

$$\mathcal{A}(^3P_1) = \frac{1}{\sqrt{3}}\frac{1}{\sqrt{M_B}}\sqrt{\frac{3}{8\pi}} R_P'(0)\epsilon_{\alpha\beta\gamma\delta}\frac{p^\gamma}{M_B}\, \mathrm{Tr}\left[\frac{1}{2}\mathcal{O}^\alpha(0)\gamma^\beta(\not{p} - M_B) - \mathcal{O}(0)\gamma^\alpha\gamma^\beta\frac{\not{p}}{M_B}\right]\varepsilon^\delta(p) \ , \tag{2.15}$$

$$\mathcal{A}(^3P_2) = \frac{1}{\sqrt{3}}\frac{i}{\sqrt{M_B}}\frac{1}{2}\sqrt{\frac{3}{4\pi}} R_P'(0)\, \mathrm{Tr}\big[\mathcal{O}^\alpha(0)\gamma^\beta(\not{p} - M_B)\big]\varepsilon_{\alpha\beta}(p) \ . \tag{2.16}$$

Later in this study, we will focus on the phenomenology of η_t, ψ_t, χ_{t0}, and χ_{t1}, the branching ratios of whose annihilation decay modes are summarized in Table 2 with the detailed corresponding formulas listed in Appendix A (see also Refs. [3, 52]). Here we take the massless limits for the fermions, and thus the fermionic decay modes of η_t and χ_{t0}, whose couplings to fermion pairs are proportional to the fermions masses, become negligible, with the exception of the $\eta_t \to b\bar{b}$ decay, for which we retain the non-zero bottom quark mass during the calculation. Note that all annihilation decay modes have partial widths that are significantly smaller than the intrinsic decay width Γ, and some of them are prohibited by J^{PC} conservation and thus have exactly zero partial widths. We will discuss the sensitivity of toponium states in some of these channels at the LHC and future colliders in Section 3.

2.3 Production

To calculate the production cross sections of toponia, one can use the projection method by modifying the kinematics accordingly and then applying the same formulas as in Eqs. (2.11)-(2.16). For example, the gluon fusion production cross section of an exactly on-shell η_t at the

decay mode (branching ratio)	η_t (0^{-+})	ψ_t (1^{--})	χ_{t0} (0^{++})	χ_{t1} (1^{++})
W^+W^-	2.42×10^{-4}	9.96×10^{-4}	1.28×10^{-6}	1.45×10^{-6}
ZZ	1.22×10^{-5}	9.29×10^{-6}	1.70×10^{-7}	1.47×10^{-8}
ZH	1.02×10^{-3}	1.38×10^{-5}	0	9.84×10^{-7}
HH	0	0	4.34×10^{-6}	0
$\gamma\gamma$	1.78×10^{-5}	0	2.65×10^{-8}	0
γH	0	1.14×10^{-4}	0	0
γZ	3.94×10^{-6}	1.32×10^{-4}	6.47×10^{-9}	1.15×10^{-10}
$\nu\bar{\nu}$	-	1.30×10^{-6}	-	8.62×10^{-9}
$\ell^+\ell^-$	-	1.45×10^{-5}	-	4.34×10^{-9}
$u\bar{u}, c\bar{c}$	-	2.47×10^{-5}	-	1.49×10^{-8}
$d\bar{d}, s\bar{s}$	-	1.14×10^{-5}	-	1.91×10^{-8}
$b\bar{b}$	7.36×10^{-8}	8.54×10^{-4}	-	3.34×10^{-8}
gg	4.58×10^{-3}	0	6.81×10^{-6}	0
ggg	0	2.77×10^{-5}	0	0

Table 2: The branching ratios of the $t\bar{t}$-annihilation decay modes of η_t, ψ_t, χ_{t0}, and χ_{t1}. Some decay modes are prohibited by J^{PC} conservation and thus have exactly zero partial widths. Here we ignore the fermion masses, and thus the fermionic decay widths of η_t and χ_{t0} are negligible, denoted as "-", except for $\eta_t \to b\bar{b}$, for which we explicitly include the non-zero bottom quark mass in the calculation. For the results with non-zero fermion masses, we refer to Refs. [3, 52].

parton level is given by

$$\hat{\sigma}(gg \to \eta_t)_{\text{on-shell}} = \frac{\pi^2 \alpha_s^2}{3M\hat{s}} |R_S(0)|^2 \delta(\hat{s} - M^2) \ , \tag{2.17}$$

where $\sqrt{\hat{s}}$ is the parton-level center-of-mass energy. Alternatively, one can also include the finite-width effect by using the Breit-Wigner (B-W) formula, which gives

$$\hat{\sigma}(gg \to \eta_t)_{\text{B-W}} = \frac{\pi \alpha_s^2}{3M^2\Gamma\hat{s}} |R_S(0)|^2 \frac{\Gamma^2/4}{(\sqrt{\hat{s}} - M)^2 + \Gamma^2/4} \ . \tag{2.18}$$

In general, the projection method is an appropriate way to compute processes involving bound states, as long as the magnitude of the relative momentum between the constituent quarks $|\vec{q}|$ is much smaller than the bound-state mass M, which is usually the case in reality for the production of heavy quarkonia near the threshold [81]. For simplicity, we will use this method to estimate the production cross sections in the sensitivity study in Section 3.

Nevertheless, the projection method ignores the interplay between the continuous $t\bar{t}$ and bound-state toponium production mechanisms, which is important when it comes to scrutinizing

the differential cross sections constructed from measuring their identical decay products. To incorporate this interplay into the calculations, one can turn to the "Green function method" [6–8, 15, 29, 72, 82], which is based on the optical theorem and accounts for the enhancement near the threshold by multiplying the continuous production cross section by the ratio of the imaginary part of the bound-state Green function to that of the free Green function. For instance, the gluon fusion production cross section of $bW^+\bar{b}W^-$ through the S-wave color-singlet toponium states can be calculated via [8, 72, 82] [2]

$$\hat{\sigma}(gg \to t\bar{t} \to bW^+\bar{b}W^-)_S = \hat{\sigma}(gg \to t\bar{t} \to bW^+\bar{b}W^-)_{S,\text{tree}} \frac{\text{Im}[G(r,E)]_{r=0}}{\text{Im}[G_0(r,E)]_{r=0}} \ , \tag{2.19}$$

where $\sigma_{S,\text{tree}}$ is the Born-level continuous production cross section through on-shell $t\bar{t}$, and G_0 and G denote the free and bound-state Green functions of the $t\bar{t}$ system, respectively. The bound-state Green function G is solved from the following Schrödinger equation,[3]

$$\left[\frac{\nabla^2}{m_t} - V(r) + z\right] G(\vec{r}, z) = \delta^3(\vec{r}), \quad z = E + i\Gamma_t \ , \tag{2.20}$$

where we approximate the QCD potential $V(r) \approx V_{\text{Coul}}(r) = -C_F \alpha_s^{\text{Coul}}/r$. The analytic solution to Eq. (2.20) is given by [83]

$$G(r,E) = \frac{m_t^2}{4\pi} a\, \Gamma\left(-\frac{ia}{2\sqrt{z'}}\right) e^{i\sqrt{z'}\rho}\, U\left(1 - \frac{ia}{2\sqrt{z'}}, 2, -2i\sqrt{z'}\rho\right) \ , \tag{2.21}$$

where we use the dimensionless quantities $\rho = m_t r$, $z' = z/m_t$, and $a = C_F \alpha_s^{\text{Coul}}$. Here, $\Gamma(x)$ is the gamma function and $U(\mathfrak{a}, \mathfrak{b}, x)$ is the Tricomi confluent hypergeometric function. When $a \to 0$, one retrieves the free Green function G_0,

$$G_0(r,E) = -\frac{m_t^2}{4\pi} \frac{e^{i\sqrt{z'}\rho}}{\rho} \ . \tag{2.22}$$

When $r \to 0$, G has an asymptotic behavior,

$$\begin{aligned} \lim_{r\to 0} G(r,E) \to \frac{m_t^2}{4\pi}\Bigg[&-\frac{1}{\rho} + a\log\rho - 2ia\pi + a\log\left(-2i\sqrt{z'}\right) \\ &+ \psi^{(0)}\left(1 - \frac{ia}{2\sqrt{z'}}\right) + 2\gamma_E a - a - i\sqrt{z'}\Bigg] \ , \end{aligned} \tag{2.23}$$

where $\psi^{(n)}(x)$ is the n-th derivative of the digamma function. Consequently, one can define the S-wave Sommerfeld enhancement factor as

$$\mathcal{S}_S(E) \equiv \frac{\text{Im}[G(r,E)]_{r=0}}{\text{Im}[G_0(r,E)]_{r=0}} = \frac{\text{Im}\left[-a\log\left(-2i\sqrt{z'}\right) - a\,\psi^{(0)}\left(1 - i\frac{a}{2\sqrt{z'}}\right) + i\sqrt{z'}\right]}{\text{Im}\left[i\sqrt{z'}\right]} \ . \tag{2.24}$$

[2] The color-octet channel is subleading around the threshold [8].

[3] One can also apply the Green function method in the momentum space as studied in Refs. [13, 14], which is useful for Monte Carlo simulations of kinematic observables.

It is worth noting that the denominator in Eq. (2.24) will in general cancel the kinematic factor $\sqrt{1-4m_t^2/\hat{s}}$ in the cross section formula when $\Gamma_t \to 0$, allowing us to extend the distribution of differential cross section $\mathrm{d}\sigma/\mathrm{d}m_{t\bar{t}}$ below the threshold of $2m_t$ without inducing an imaginary number, as shown in Ref. [7].

Here we demonstrate the consistency between the Green function and projection methods regarding the production cross section $\sigma(pp \to \eta_t)$. For the Green function method, we take $V_{\mathrm{Coul}}(r)$ with $\alpha_s^{\mathrm{Coul}} = 0.189$ as obtained from matching the S-wave binding energy with $\mu_R = 1/r$ in Section 2.1, while for the projection method, we use the same setup as in Section 2.2 when studying the annihilation decays and adopt the B-W formula. We compute the differential cross section $\mathrm{d}\sigma(pp \to \eta_t)/\mathrm{d}m_{t\bar{t}}$ with both methods and show the results in Figure 2. One can see that the two methods provide comparable values around and below the threshold. On the other hand, the Green function method predicts an additional continuum spectrum above the threshold. Next, we define the "resonance" region in the $t\bar{t}$ invariant mass spectrum as $m_{t\bar{t}} \in [M_{\eta_t} - \Gamma, M_{\eta_t} + \Gamma] = [342.08 - 2.84, 342.08 + 2.84]$ GeV and integrate the differential cross section over this interval to obtain the proton-level production cross section $\sigma(pp \to \eta_t)_{\mathrm{Green}} =$ 7.08 pb, which is compatible with the experimental result of $\sigma(pp \to \eta_t) = 8.8^{+1.2}_{-1.4}$ pb reported in Ref. [62] within $2\,\sigma$. On the other hand, the projection method gives the cross section of $\sigma(pp \to \eta_t)_{\mathrm{Projection}} = 6.89$ pb, which is also compatible with both the Green function and the experimental results. We note here that the experimental measurements reported at the LHC consist of both the quasi-bound state and above-threshold-continuum contributions. Also, the K-factor is very close to one and thus does not influence the results here much, as mentioned in Ref. [8]. Moreover, the differential cross section derived from the Green function method is only reliable around the $m_{t\bar{t}} = 2m_t$ threshold, where the non-relativistic assumption made in Eq. (2.20) is justified. We follow the upper bound $m_{t\bar{t}} < 350$ GeV used in several studies based on non-relativistic QCD (NRQCD) to truncate our calculation, as suggested in Refs. [12, 13]. To extend the applicable window to larger $m_{t\bar{t}}$, we refer to Ref. [8]. In general, one can also generalize the Green function method to the P-wave case; however, as we will demonstrate in Section 3.3, the production cross sections of P-wave toponia at future colliders are too small to be sensitive to experimental searches, and thus we only present the corresponding comparison in Appendix B.

While a detailed review and rigorous application of the Green function method is beyond the scope of this study, we note here some caveats of the method that are still under active research (see for example Refs. [5, 12, 51, 84–86]). Despite the intention of the Green function method to incorporate bound-state effects into the calculation of the $m_{t\bar{t}}$ spectrum, there exist inevitable scattering-state contributions to its final outcome that need to be properly subtracted and matched. There are two main reasons behind this [6]: 1. While in the $\Gamma_t \to 0$ limit, one can safely rely on the Green function method to resum the total cross section close to the threshold expanded in $(\alpha_s/v)^n$ [72], v being the top quark velocity in the $t\bar{t}$ rest frame, in reality because of the large Γ_t, a broad "resonance" across the entire threshold regime will receive such corrections. 2. Unique to hadron colliders, additional radiation of gluons becomes significant near the threshold and can be resummed in terms of the expansion in $(\alpha_s^2 \ln^2 v)^n$, which should also be taken into account when performing higher-order corrections to both the Coulomb-gluon exchange effects and the fixed-order calculations [6]. Consequently, it is important to match the results of the Green function method and fixed-order calculations to properly distinguish

between the bound-state and the scattering-state contributions to the total cross section near the threshold. Before then, one cannot claim with certainty whether the $t\bar{t}$ threshold enhancements measured by CMS and ALTAS actually imply the existence of η_t.

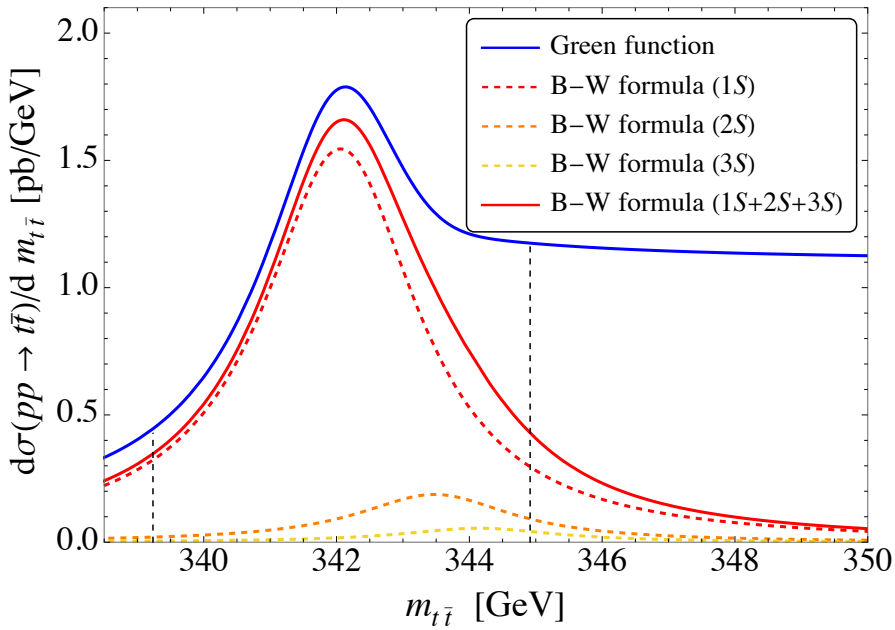

Figure 2: The $\mathrm{d}\sigma(pp \to \eta_t)/\mathrm{d}m_{t\bar{t}}$ distributions at the 13-TeV LHC calculated using the leading-order Green function method (blue) and the B-W formula with the first three $\eta_t(nS)$ states superposed (red). The two dashed vertical lines represent $m_{t\bar{t}} = M_{\eta_t} \pm \Gamma$ with $M_{\eta_t} = 342.08$ GeV and $\Gamma = 2.84$ GeV, respectively, between which we identify the $t\bar{t}$ system to be on "resonance". We also show the individual nS resonances with $n = 1$ (red), $n = 2$ (orange), and $n = 3$ (yellow) in dashed curves.

3 Sensitivity of toponium states at the LHC and future colliders

In this section, we discuss the discovery sensitivity of η_t, ψ_t, χ_{t0}, and χ_{t1} at the LHC and future colliders, including the HL-LHC and FCC-ee. For the associated annihilation decays and production cross sections, we calculate them using the projection method reviewed in Sections 2.2 and 2.3 and ignore the K-factors unless otherwise specified. A brief summary of the proposed specs of the mentioned future colliders is given in Table 3.

3.1 η_t

We begin our discussion of η_t with the recent measurement performed by CMS in Ref. [62], which assumes $m_t = m_t^{\rm MC} = 172.5$ GeV and $M_{\eta_t} = 343$ GeV (and thus implies $E_{\rm bind} = -2$ GeV) and reports $\sigma(pp \to \eta_t) = 8.8^{+1.2}_{-1.4}$ pb. ATLAS also performed the same study and reported

future collider	$\sqrt{s}$	expected integrated luminosity ($\mathcal{L}$)
HL-LHC	14 TeV	3 ab^{-1}
FCC-ee	360 GeV	2.70 ab^{-1}
	340-350 GeV	0.42 ab^{-1}

Table 3: A brief summary of the proposed specs of the HL-LHC [87] and FCC-ee [76, 77].

$\sigma(pp \to \eta_t) = 9.3^{+1.4}_{-1.3}$ pb [63]. In both studies, the quasi-bound-state mass M_{η_t} is treated as a fixed value rather than being fitted from the data. Both collaborations have in fact observed an excess in $t\bar{t}$ production near the threshold region. As shown in Figure 2 and calculated more precisely in Ref. [51], the signal receives contributions from both quasi-bound states and the continuum. However, the current experimental analyses use bins of the $t\bar{t}$ invariant mass that are too large to resolve these two components separately. On the other hand, the observed excess provides a strong hint for the existence of a quasi-bound state near the threshold, given the comparable predicted magnitude of the toponium contribution within the NRQCD framework.

To see what the experimental results might imply, we show the contours derived from varying $\kappa \equiv \mu_R \times r$ on the M_{η_t}–$\sigma(pp \to \eta_t)$ plane with m_t chosen to be 172.4 GeV, $172.4 + 0.7$ GeV, and $172.4 - 0.7$ GeV according to the the measured top quark pole mass reported in Ref. [68] [4] in Figure 3, in which we also show the experimental results at 1σ and 95% confidence level (CL). Again, we ignore the K-factor since it is close to one as discussed in Ref. [8]. One can see that the theoretical contours cover a large area of the M_{η_t}–σ plane under the variation of m_t and κ, signaling that the experimental result should be further improved to properly reflect these uncertainties in the predicted value of M_{η_t}. Moreover, while the theoretical predictions here are obtained with the MSTW 2008 NNLO PDF [89], it is also important to consider the uncertainties arising from different PDF choices, although we have checked that most will agree within systematic errors. Therefore, it remains an open issue for experimental searches to properly account for the underlying theoretical uncertainties in the η_t measurement to test the SM QCD, which could then later be used to more rigorously probe certain BSM physics, as we will discuss with an explicit example in Section 4.

Given the strong hint of the existence of η_t in the gluon fusion channel via the individual top decays, it is valid to ask what other avenues we can use to study its properties. One possibility is to probe its next-to-leading annihilation decay to ZH, which has a branching ratio of roughly 1.02×10^{-3}. Along with the measured production cross section $\sigma(pp \to \eta_t) = 8.8$ pb, one obtains $\sigma(pp \to \eta_t \to ZH) = 8.98$ fb at the 13-TeV LHC. In the following, we perform the Monte Carlo studies, including those for the corresponding backgrounds, using `MadGraph5_aMC@NLO` [91] at the parton level, `Pythia 8` [92] for parton showering and hadronization, and `Delphes 3` [93] for detector effects. We use the model provided in Ref. [52] to simulate the processes and reconstruct the Z boson from the dileptonic events $\ell^+\ell^-$ and the H boson from $b\bar{b}$. In this channel, the main backgrounds come from the continuum $Zb\bar{b}$ and the dileptonic decay of $pp \to t\bar{t}$ [90]. In addition, the production of continuum $pp \to ZH$ is also considered. The cuts applied in the analysis are as follows, with their efficiencies reported in Table 4: We select the events that

[4] For a detailed discussion of different definitions of the top quark mass and how they can be measured from experiments, see Ref. [88].

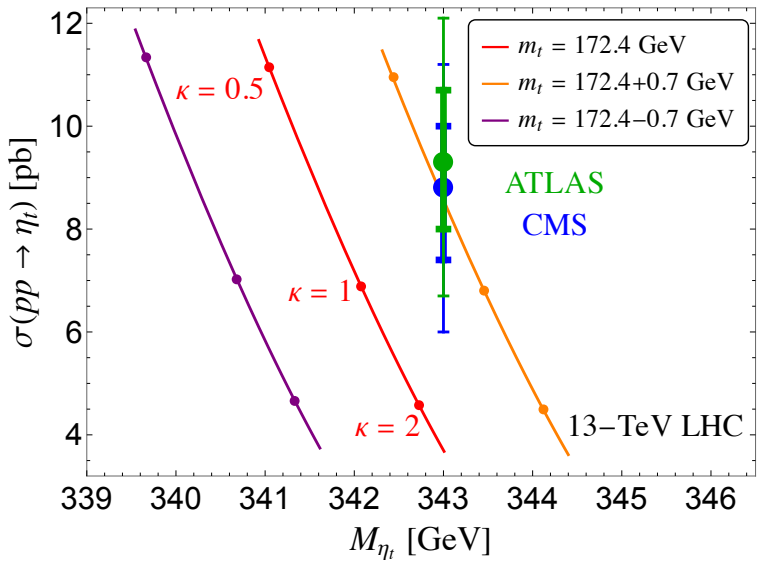

Figure 3: The theoretical contours on the M_{η_t}–$\sigma(pp \to \eta_t)$ (13-TeV LHC) plane derived from varying $\kappa \equiv \mu_R \times r$ with $m_t = 172.4$ GeV (red), $m_t = 172.4 + 0.7$ GeV (orange), and $m_t = 172.4 - 0.7$ GeV (purple), respectively, according to the pole mass $m_t^{\rm pole} = 172.4 \pm 0.7$ GeV reported in Ref. [68]. We also present the experimental results reported in Ref. [62] (blue) and Ref. [63] (green), respectively, at 1σ (thick lines) and 95% CL (thin lines) assuming $m_t = m_t^{\rm MC} = 172.5$ GeV and $M_{\eta_t} = 343$ GeV. We neglect the K-factor since it is close to one as discussed in Ref. [8].

satisfy the basic cuts on the transverse momenta and pseudo-rapidities, $p_T^{\ell,j} > 25$ GeV and $|\eta_{j,\ell}| < 2.5$. For ZH reconstruction, we require at least two b-jets and two leptons in the final state. The Z boson is reconstructed by requiring 77 GeV $< m_{\ell\ell} <$ 101.2 GeV, and the H boson 100 GeV $< m_{b\bar{b}} <$ 145 GeV, following Ref. [90]. To suppress the $t\bar{t}$ background, we impose a missing transverse energy cut $E_T^{\rm miss}/\sqrt{H_T} < 1.15\sqrt{\rm GeV}$, where H_T is the scalar sum of the transverse momenta of the leptons and b-jets. We then select the invariant mass window

process	$\eta_t \to ZH$	$Zb\bar{b}$	$t\bar{t}$	ZH
cross section×BR [fb]	0.32	7.52×10^4	2.76×10^4	22.47
Z, H reconstruction	7.87%	0.15%	1.81%	4.91%
$E_T^{\rm miss}/\sqrt{H_T} < 1.15\sqrt{\rm GeV}$	4.28%	0.07%	0.10%	2.99%
$310 < m_{ZH}/{\rm GeV} < 370$	3.81%	0.01%	0.03%	0.53%
fiducial cross section [fb]	0.012	6.775	8.280	0.118

Table 4: The signal and backgrounds of the search for $pp \to \eta_t \to (Z \to \ell^+\ell^-)(H \to b\bar{b})$. Note that the backgrounds coming from the dileptonic decay of the continuum $t\bar{t}$ and the dominant $Zb\bar{b}$ from Z+heavy flavors are included following Ref. [90].

310 GeV $< m_{ZH} <$ 370 GeV to enhance the signal-to-background contrast. Consequently, assuming an integrated luminosity of 3 ab^{-1} at the HL-LHC, we find the significance to be only 0.17σ, which is mainly suppressed by the large backgrounds coming from $Zb\bar{b}$ and $t\bar{t}$. Assuming the same efficiencies, we estimate that the 2σ exclusion upper bound on the production cross section for a pseudoscalar boson decaying into ZH is around 500 fb, consistent with the $\sim$ 300 fb limit shown in Ref. [90] which additionally includes the $Z \to \nu\nu$ channel. Moreover, the $\eta_t \to W^+W^-$ decay channel is also highly suppressed according to the W^+W^- resonance searches to date. For example, Ref. [94] reports a sensitivity of around 500 fb for the resonance production of W^+W^- at 350 GeV, while the predicted $\sigma(pp \to \eta_t \to W^+W^-)$ is only about 2 fb. Therefore, we conclude that neither $\eta_t \to ZH$ nor $\eta_t \to WW$ can be probed at the current LHC or the future HL-LHC.

Another promising channel is $gg \to \eta_t b\bar{b}$, an example Feynman diagram of which is shown in Figure 5(a). Taking into account only the QCD-induced diagrams and using the projection method, one obtains $\sigma(pp \to \eta_t b\bar{b}) = 0.37$ pb at the 13-TeV LHC. Compared to the continuum background with $\sigma(pp \to t\bar{t}b\bar{b}) = 16.3$ pb calculated using Monte Carlo simulations at tree level, the ratio between them is of the same order of magnitude as that in the direct η_t search. Therefore, this process is likely to be probed at both the current LHC and the future HL-LHC, which we explore in the dileptonic decay channel of the top quark pairs in what follows.

The $t\bar{t}b\bar{b}$ channel has been studied at the LHC (see for example Ref. [95]). Here we use a simplified pseudoscalar model for η_t to simulate the signal kinematics but stick to the cross section calculated using the projection method reported above in order to avoid potential issues related to the effective vertices, as we will discuss in Section 5. We apply the basic cuts $p_T^{\ell,j} >$ 25 GeV and $|\eta_{j,\ell}| < 2.5$ and require at least two leptons and four jets in the final state, with at least three of the jets tagged as b-jets. The neutrino momenta are reconstructed using four-momentum conservation together with the on-shell conditions for W and t, after which we select from the possible solutions the one that gives the smallest $m_{t\bar{t}}$. Then, we impose the mass window cut 330 GeV $< m_{t\bar{t}} <$ 370 GeV around the η_t mass. Finally, we also study the angular observables $c_{\rm hel}$ and $c_{\rm han}$ defined in the CMS and ATLAS studies for $t\bar{t}$ threshold production [62, 63] and find that the cut $c_{\rm hel} > 1/3$ improves the significance by only about 4%, which we still include in our analysis.

The signal and background cross sections and efficiencies are summarized in Table 5, and the reconstructed $m_{t\bar{t}}$ distributions are shown in Figure 4. Together with the dileptonic branching ratios and including the K-factor of 1.77 [96], the significance is estimated to be about 6.1σ at the HL-LHC, making it a promising channel that can serve as complementary evidence that the pseudoscalar resonance measured at the LHC indeed originates from the quasi-bound state effects of the $t\bar{t}$ system, rather than from a new-physics pseudoscalar A, such as in the two-Higgs-doublet model. A new-physics state A can have an $Ab\bar{b}$ coupling that is independent of QCD dynamics, and the process $pp \to Ab\bar{b}$ can be produced through diagrams involving this b-quark coupling. In contrast, $pp \to \eta_t b\bar{b}$ proceeds through gluon couplings and is predominantly determined by QCD interactions, up to minor electroweak contributions that we find negligible from our calculations. Therefore, if the HL-LHC measures a cross section consistent with the predicted value, it would provide strong evidence that the pseudoscalar resonance associated with the $t\bar{t}$ system indeed exists.

On the other hand, η_t is less likely to be directly produced at lepton colliders due to its J^{PC}

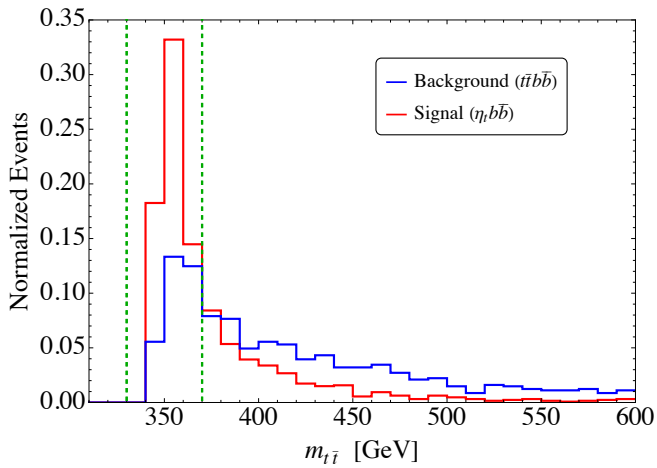

Figure 4: The normalized $m_{t\bar{t}}$ distributions obtained from the reconstructed $t\bar{t}$ events for the $\eta_t b\bar{b}$ signal (red) and the $t\bar{t}b\bar{b}$ background (blue). The green dashed lines indicate the selection window 330 GeV $< m_{t\bar{t}} <$ 370 GeV.

property, which prohibits its singular production through the process $e^+e^- \to \eta_t$ given the tiny electron mass. Some other possible production mechanisms include $e^+e^- \to \eta_t\gamma$, $e^+e^- \to \eta_t Z$, and $e^+e^- \to \eta_t H$ [see Figure 5(b) for an example Feynman diagram of $e^+e^- \to \eta_t\gamma$], which we explore using the projection method in what follows. Since the currently proposed $\sqrt{s}$ of the future lepton colliders listed in Table 3 are all only slightly above the $t\bar{t}$ threshold, we only consider the $e^+e^- \to \eta_t\gamma$ process. Taking $\sqrt{s} = 360$ GeV, which is proposed for the FCC-ee, one obtains $\sigma(e^+e^- \to \eta_t\gamma) = 8.87 \times 10^{-3}$ fb after applying the photon cuts $p_T^\gamma > 10$ GeV and $|\eta_\gamma| < 3.0$. Compared to the continuous background with the same cuts applied, which has $\sigma(e^+e^- \to t\bar{t}\gamma) = 8.57$ fb according to Monte Carlo simulations, it is clear that η_t is unlikely to be probed via this process and thus at lepton colliders in general.

process	$\eta_t b\bar{b}$	$(t\bar{t}b\bar{b})_{\rm SM}$
cross section$\times$ BR [fb]	16.8	1313
basic selection	17.75%	15.00%
$t, \bar{t}$ reconstruction	2.57%	1.81%
$330 < m_{t\bar{t}}/\text{GeV} < 370$	1.68%	0.51%
$c_{\rm hel} > 1/3$	1.00%	0.16%
fiducial cross section [fb]	0.17	2.11

Table 5: The cross sections and efficiencies obtained from the study of $\eta_t b\bar{b}$ production, including those of the signal and the continuum background $t\bar{t}b\bar{b}$. The branching ratio (BR) used here for both the signal and background corresponds to that of the dileptonic decay of $t\bar{t}$.

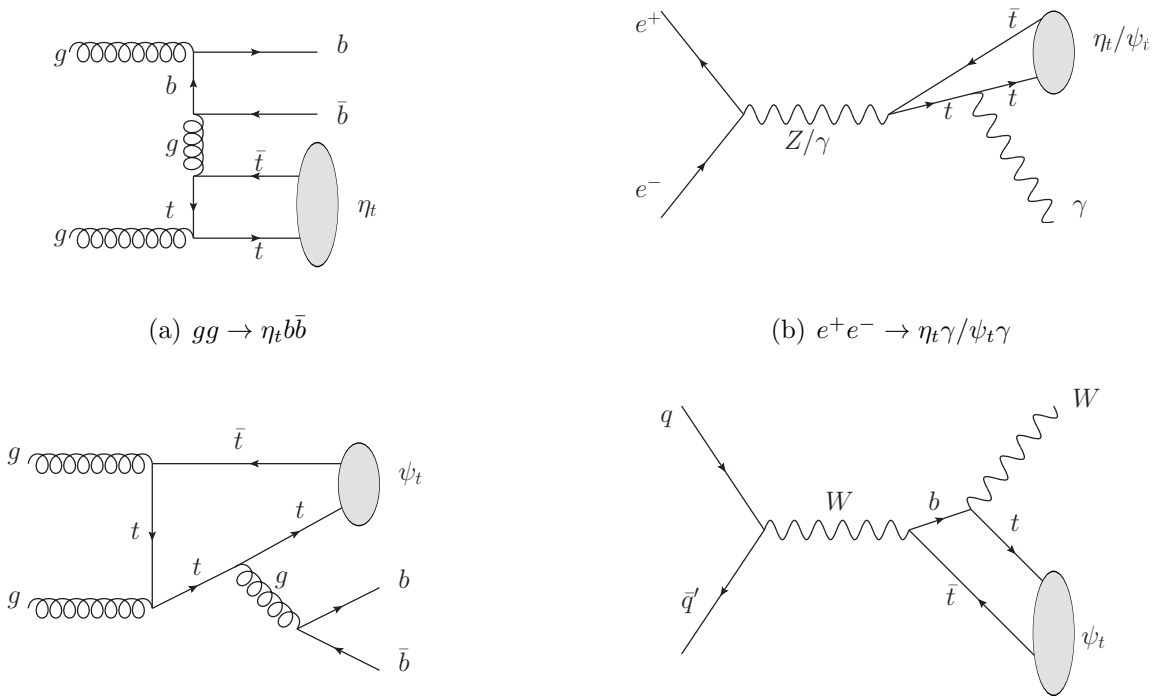

(a) $gg \to \eta_t b\bar{b}$

(b) $e^+e^- \to \eta_t\gamma/\psi_t\gamma$

(c) $gg \to \psi_t b\bar{b}$

(d) $q\bar{q}' \to \psi_t W$

Figure 5: Example Feynman diagrams of the specified processes considered in this study.

3.2 ψ_t

For the ψ_t state, since it cannot be produced singularly through gluon fusion as prohibited by the Landau-Yang theorem [73, 74], we consider other (associated) production mechanisms: $gg \to \psi_t g$, $gg \to \psi_t b\bar{b}$, and $q\bar{q}' \to \psi_t W$ at the LHC and $e^+e^- \to \psi_t$ at lepton colliders. For the first process, the parton-level associated production cross section is given by

$$\hat{\sigma}(gg \to \psi_t g) = \frac{10\pi\alpha_s^3}{9M\hat{s}^2(\hat{s}-M^2)^2(\hat{s}+M^2)^3}|R_S(0)|^2\Bigg[(\hat{s}^2-M^4)(2\hat{s}^3+M^2\hat{s}^2+4M^4\hat{s}+M^6) - 2M^4\hat{s}(M^4+2M^2\hat{s}+5\hat{s}^2)\log\left(\frac{\hat{s}}{M^2}\right)\Bigg], \tag{3.1}$$

which gives the proton-level cross section $\sigma(pp \to \psi_t g) = 73.3$ fb at the 13-TeV LHC. Here, $M = M_{\psi_t}$. This result is overwhelmed by the continuous production cross section $\sigma(pp \to t\bar{t}+j) = \mathcal{O}(10^3)$ pb. For the second process, the cross section given by the projection method using the QCD-induced diagrams [see for example Figure 5(c)] is $\sigma(pp \to \psi_t b\bar{b}) \sim \mathcal{O}(2)$ fb at the 13-TeV LHC, while the electroweak contribution is $\sim \mathcal{O}(0.3)$ fb, the combined result of which is significantly prevailed by both the continuous background with $\sigma(pp \to t\bar{t}b\bar{b}) = 16.3$ pb and the η_t-induced background with $\sigma(pp \to \eta_t b\bar{b}) = 0.37$ pb. Finally, for the third process [see for example Figure 5(d)], the associated cross section is $\sigma(pp \to \psi_t W) = 0.09$ fb at the 13-TeV LHC, which is again overwhelmed by the continuous background with $\sigma(pp \to t\bar{t}W) = 369$ fb as reported by Monte Carlo studies. Therefore, we conclude that it is unlikely to probe ψ_t at

both the current LHC and the future HL-LHC.

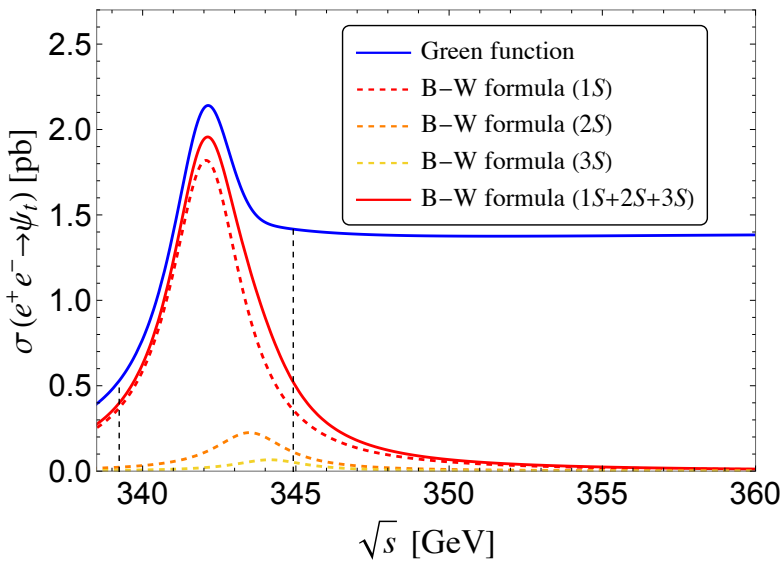

Figure 6: The cross section $\sigma(e^+e^- \to t\bar{t})$ as a function of $\sqrt{s}$ calculated using both the Green function method (blue) and the B-W formula (red). The two vertical dashed lines denote $m_{t\bar{t}} = M_{\psi_t} \pm \Gamma$, respectively, between which we identify the "resonance" region. We also show the individual nS resonances with $n = 1$ (red), $n = 2$ (orange), and $n = 3$ (yellow) in dashed curves, as in Figure 2.

On the other hand, the production of ψ_t at lepton colliders has been widely studied in the literature (see for example Refs. [18, 20, 27, 29]). In particular, FCC-ee [76, 77] proposes to run at the $t\bar{t}$ threshold around $\sqrt{s} \sim 360$ GeV, which would most likely further cover the mass pole of ψ_t (together with other excited states) around $2m_t$, and thus we discuss the prospect of ψ_t measurements at future lepton colliders. First of all, we calculate the production cross section $\sigma(e^+e^- \to \psi_t)$ around $\sqrt{s} = M_{\psi_t}$ using both the Green function method and the B-W formula in Figure 6, based on which we further estimate the significance of ψ_t discovery through its intrinsic decay to $W^+W^-b\bar{b}$ using the B-W formula. The continuous background $e^+e^- \to W^+W^-b\bar{b}$ has a cross section of 30.5 fb at $\sqrt{s} = M_{\psi_t}$ and increases rapidly after $\sqrt{s}$ passes through $2m_t$. Assuming the reconstruction efficiency of the $t\bar{t}$ final state to be above 10%, the integrated luminosity to be 1 ab^{-1}, and using both the dileptonic and semi-leptonic final states from top decays, one could easily discover ψ_t at $\sqrt{s} = M_{\psi_t}$.

Moreover, in the recent Ref. [40], it is claimed that the two-body annihilation decays of ψ_t could be discovered with a significance of over $5\,\sigma$ at a lepton collider by measuring the cross section ratio $R_b \equiv \sigma(e^+e^- \to b\bar{b})/\sum_{q=u,d,s,c,b} \sigma(e^+e^- \to q\bar{q})$ at a few different $\sqrt{s}$ points. The main idea is to capture the interference effect caused by the ψ_t-mediated diagrams when $\sqrt{s}$ passes from below M_{ψ_t} to above M_{ψ_t}. As a result of this interference, $R_b(\sqrt{s})$, which would only be a flat line around $\sqrt{s} = M_{\psi_t}$ if only the γ- and Z-poles were present, will manifest an interference pattern that can facilitate the measurement of the ψ_t-pole. One major factor enabling this possibility is the relatively large annihilation decay width of $\psi_t \to b\bar{b}$ (see Table 2), owing to the W-mediated contributions, which are highly suppressed for down-type quarks of

the other generations but not for bottom quarks. Nevertheless, we note that their follow-up paper, Ref. [52], contains a sign error in the coupling $g^V_{\psi_t}$ in the interaction $\bar{b}\gamma_\mu(g^V_{\psi_t} - g^A_{\psi_t}\gamma^5)b\,\psi_t^\mu$ (their earlier paper Ref. [40] and the public model file are both correct) and also uses a larger value of α_s than in our study.

To assess the interference effects in $\psi_t \to b\bar{b},\ W^+W^-,\ \gamma Z$, we perform a simple analysis in which the significance is estimated via $S/\sqrt{B}$. Here S represents the deviation of the number of events from the SM prediction without the ψ_t quasi-bound state, which arises mainly from interference effects. We focus on a single energy point that yields the highest significance and assume that the full luminosity of 420 fb^{-1} is accumulated at that point to maximize the sensitivity.

We use the "bound state effective field theory" (BSEFT) developed in Ref. [52] to compute the cross sections along with Monte Carlo simulations, and the validity of this approach is discussed in Section 5. The interference patterns of the cross sections for the three processes are shown in Figure 7, and the formulas for $\sigma(e^+e^- \to b\bar{b}, \gamma Z)$ are listed in Appendix A. We present the relevant effective couplings as well as the projected sensitivities for each process in the following.

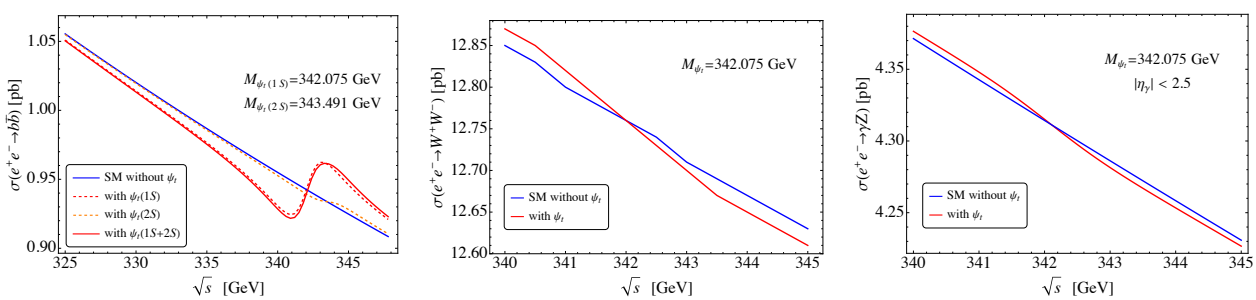

Figure 7: The cross sections of $e^+e^- \to b\bar{b}$ (left), W^+W^- (middle), and γZ (right) predicted by the SM without including the ψ_t contribution (blue) and including ψ_t (red) around the ψ_t mass. The $b\bar{b}$ channel shows the largest relative difference between the cases with and without ψ_t, so we also include the effect of $\psi_t(2S)$ for comparison.

For the $b\bar{b}$ channel, the bound state effective couplings in $\mathcal{L}_{\psi_t bb} = \bar{b}\gamma_\mu(g^V_{\psi_t b} - g^A_{\psi_t b}\gamma^5)b\psi_t^\mu$ are

$$g^V_{\psi_t b} = \sqrt{\frac{(C_F\alpha_s)^3\pi}{3}}\frac{\alpha_{\rm EM}}{12}\left\{\frac{m_t^2}{s_w^2}\left[\frac{4(8c_w^2+1)s_w^2-9}{c_w^2(4m_t^2-m_Z^2)} - \frac{3}{m_t^2+m_W^2} - \frac{3}{m_W^2}\right] - 8\right\}\ ,$$
$$g^A_{\psi_t b} = -\sqrt{\frac{(C_F\alpha_s)^3\pi}{3}}\frac{\alpha_{\rm EM}\,m_t^2}{4s_w^2}\left[\frac{3-8s_w^2}{c_w^2(4m_t^2-m_Z^2)} + \frac{1}{m_t^2+m_W^2} + \frac{1}{m_W^2}\right]\ , \tag{3.2}$$

where all three particles, ψ_t, b, and $\bar{b}$, are on shell and $M_{\psi_t} \approx 2m_t$. Here $\alpha_{\rm EM}$ is the electric fine structure constant, $c_w \equiv \cos\theta_w$ and $s_w \equiv \sin\theta_w$ with θ_w being the weak angle. In addition to the intrinsic $(b\bar{b})_{\rm SM}$ background, we also include the $(b\bar{b}jj)_{\rm SM}$ background. Other backgrounds, including mis-tagged events from jj and $b\bar{b}b\bar{b}$, are negligible as shown in Ref. [40]. Selected events are required to contain two b-tagged jets with $p_T^{b,j} > 20$ GeV and $|\eta_{b,j}| < 3$. The optimal $\sqrt{s}$ is found to be 343.5 GeV for $M_{\psi_t} = 342$ GeV, where a significance of $14\,\sigma$ can be achieved with 420 fb^{-1}. The corresponding cross sections and selection efficiencies are shown in Table 6.

Given that the large significance arises from interference in this channel, we also evaluate the contribution from $\psi_t(2S)$, as shown in Figure 7. It can be seen that the interference effect is dominated by the $\psi_t(1S)$ state.

process	$\psi_t \to b\bar{b}$	$(b\bar{b})_{\rm SM}$	$(b\bar{b}jj)_{\rm SM}$
cross section× BR [fb]	961.2	933.7	298.2
efficiency	69.09%		48.44%
fiducial cross section [fb]	664	645	144.4

Table 6: The cross sections and efficiencies obtained from the study of $\psi_t \to b\bar{b}$, including those of the signal and the backgrounds. Here, $M_{\psi_t} = 342$ GeV and $\sqrt{s} = 343.5$ GeV.

To search for the $\psi_t \to W^+W^-$ decay, the relevant interactions are given by

$$\begin{aligned}\mathcal{L}_{\psi_t WW} = \Big\{ & i g_{\psi_t WW,1} \left[(\partial_\sigma W^-_\mu)W^{+\sigma} - (\partial_\sigma W^+_\mu)W^{-\sigma}\right] + \frac{i}{2} g_{\psi_t WW,2} \left[(\partial_\mu W^-_\sigma)W^{+\sigma} - (\partial_\mu W^+_\sigma)W^{-\sigma}\right] \\ & g_{\psi_t WW,3}\epsilon_{\mu\nu\rho\sigma} \left[(\partial^\nu W^{-\rho})W^{+\sigma} - (\partial^\nu W^{+\rho})W^{-\sigma}\right]\Big\}\psi_t^\mu \,, \end{aligned} \tag{3.3}$$

$$\begin{aligned} g_{\psi_t WW,1} &= \sqrt{\frac{(C_F\alpha_s)^3\pi}{3}}\frac{\alpha_{\rm EM}}{2s_w^2}\frac{-3m_t^2(4m_b^2 - 4m_W^2 + m_Z^2) + 8m_Z^2 s_w^2(m_b^2 + m_t^2 - m_W^2)}{(m_t^2 + m_b^2 - m_W^2)(4m_t^2 - m_Z^2)} \,, \\ g_{\psi_t WW,2} &= \sqrt{\frac{(C_F\alpha_s)^3\pi}{3}}\frac{\alpha_{\rm EM}}{s_w^2}\frac{-4m_Z^2 s_w^2(m_t^2 + m_b^2 - m_W^2) + 3m_t^2(m_Z^2 + 2m_b^2 - 2m_W^2 - 2m_t^2)}{(m_t^2 + m_b^2 - m_W^2)(4m_t^2 - m_Z^2)} \,, \\ g_{\psi_t WW,3} &= -\sqrt{\frac{(C_F\alpha_s)^3\pi}{3}}\frac{3\alpha_{\rm EM} m_t^2}{2s_w^2(m_t^2 + m_b^2 - m_W^2)} \,. \end{aligned} \tag{3.4}$$

We consider the fully hadronic final state, which has a subleading background from ZZ. Jets are selected with $p_T^j > 20$ GeV and $|\eta_j| < 3$. Owing to the collimated nature of the two jets from the W decay, we use the "ee_genkt_algorithm" jet-finding algorithm with $R = 1.5$ in `Delphes 3` and impose the mass window cuts $|m_j - m_W| < 10$ GeV on the single-jet events and $|m_{jj} - m_W| < 10$ GeV on the dijet events. The efficiencies of these cuts are given in Table 7. The estimated significance reaches $1.3\,\sigma$ at 340.5 GeV for a luminosity of $420\,\text{fb}^{-1}$. With improved reconstruction efficiencies, one may observe some hints of this channel at the FCC-ee.

For $\psi_t \to \gamma Z$ channel, the effective Lagrangian is $\mathcal{L}_{\psi_t ZA} = g_{\psi_t ZA}\epsilon_{\mu\nu\rho\sigma}A^{\mu\nu}Z^\rho\psi_t^\sigma$, where

$$g_{\psi_t ZA} = \sqrt{\frac{(C_F\alpha_s)^3\pi}{3}}\frac{4\,\alpha_{\rm EM}\,m_t^2}{c_w s_w(4m_t^2 - m_Z^2)} \,. \tag{3.5}$$

We examine two reconstruction strategies: the invisible decay $Z \to \nu\bar{\nu}$ and the hadronic Z decay. For the neutrino channel, the continuous background $\gamma\nu\bar{\nu}$ away from the Z-pole is negligible. The reconstructed Z four-momentum, $p_{Z,\rm recon}$, is determined from energy conservation via $E_Z = \sqrt{s} - E_\gamma$. The basic cut on the photon is $p_T^\gamma > 10$ GeV and $|\eta_\gamma| < 2.5$. We impose two additional requirements: the reconstructed Z mass must satisfy $|m_{Z,\rm recon} - m_Z| < 8$ GeV, and the most

energetic photon is required to have $p_T^\gamma > 50$ GeV. For the hadronic Z channel, we select jets with $p_T^j > 20$ GeV and $|\eta_j| < 3$. As in the W^+W^- case, the collimation of the Z decay products for some boosted Z bosons makes jet identification challenging. We therefore apply both single-jet and dijet mass window cuts, $|m_j - m_Z| < 10$ GeV and $|m_{jj} - m_Z| < 10$ GeV. The maximum significance occurs at $\sqrt{s} = 344$ GeV. The corresponding cross sections and efficiencies are summarized in Table 8. Assuming that the FCC-ee operates at this energy with 420 fb^{-1}, the expected significances are $0.54\,\sigma$ for the invisible Z decay channel and $0.80\,\sigma$ for the hadronic decay channel.

For the final channel of ψ_t, we consider the decay $\psi_t \to \gamma H$, which has a cross section of $\sigma(e^+e^- \to \psi_t \to \gamma H) = 0.26$ fb at $\sqrt{s} = M_{\psi_t}$ according to the projection method after applying the basic photon cuts $p_T^\gamma > 10$ GeV and $|\eta_\gamma| < 3$. Unlike the previous channels, the significance of this process arises primarily from the resonance itself rather than from interference, since the SM production of γH proceeds only through loop processes and is suppressed. However, for Higgs detection through the $b\bar{b}$ decay, the dominant background becomes the continuous $\gamma b\bar{b}$ production. For this channel, we require that the selected events contain at least one b-jet and pass the photon cuts mentioned above. To reconstruct the Higgs boson, we impose the mass window cut 120 GeV $< m_{b\bar{b}} <$ 128 GeV. Given the production of some boosted Higgs bosons from this process, the b-jets are often not resolved as separate jets by the detector, so we also

process	$\psi_t \to W^+W^-$	$(W^+W^-)_{\rm SM}$	$(ZZ)_{\rm SM}$
cross section$\times$ BR [fb]	5711.1	5702.2	2273.0
basic selections	87.77%		84.79%
W reconstruction	33.76%		10.26%
fiducial cross section [fb]	1924.8	1921.5	241.6

Table 7: The cross sections and efficiencies obtained from the study of $\psi_t \to W^+W^-$, including those of the signal and the backgrounds. The branching ratios (BRs) here all refer to the hadronic decay branching ratios. Here, $M_{\psi_t} = 342$ GeV and $\sqrt{s} = 340.5$ GeV.

process	$\psi_t \to \gamma Z_{\nu\bar{\nu}}$	$(\gamma Z)_{\rm SM}$	$\psi_t \to \gamma Z_{\rm hadron}$	$(\gamma Z)_{\rm SM}$
cross section$\times$ BR [fb]	851.6	850.6	2977	2973
basic selections	98.77%		86.35%	
Z reconstruction	87.32%		55.06%	
η_γ cut efficiency	59.41%		36.89%	
fiducial cross section [fb]	505.927	505.333	1098.22	1096.93

Table 8: The cross sections and efficiencies obtained from the study of $\psi_t \to \gamma Z$, including those of the signal and the backgrounds. The branching ratio (BR) corresponds to that of the neutrino decay on the left side and that of the hadronic decay on the right side, for both γZ production with and without ψ_t. The other background, $\gamma\nu\bar{\nu}$ without the Z-pole contribution, is found to be negligible. Here, $M_{\psi_t} = 342$ GeV and $\sqrt{s} = 344$ GeV.

include events with a single jet falling within this mass window, similar to the treatment for the previous channels. The most energetic photon is selected, and we further impose the cuts $|m_{\gamma H} - m_{\psi_t}| < 5$ GeV and $p_T^\gamma > 85$ GeV. The corresponding efficiencies are listed in Table 9, yielding a significance of $0.6\,\sigma$ at the FCC-ee with 420 fb^{-1}. The possible measurement of this channel relies on the capability of future experiments to inclusively reconstruct the γH final state, which, if performed efficiently, would provide another way to discover ψ_t and potentially probe the top Yukawa coupling.

process	$\psi_t \to \gamma H$	$(\gamma b\bar{b})_{\rm SM}$	$(\gamma H)_{\rm SM}$
cross section$\times$ BR [fb]	0.1382	54.69	0.0466
basic selections	69.63%	45.37%	70.38%
H reconstruction	14.43%	2.97%	14.93%
hard photon cut	8.96%	0.334%	9.62%
fiducial cross section [fb]	0.0124	0.183	0.0045

Table 9: The cross sections and efficiencies for study of $\psi_t \to \gamma H$ with signal and SM background $\gamma b\bar{b}$, γH. The branching ratio, BR, here for γH is the $H \to b\bar{b}$ branching ratio. To increase the statistics of $\gamma b\bar{b}$, we use 100 GeV $< m_{b\bar{b}} <$ 150 GeV at generation level.

3.3 χ_t

For the P-wave χ_t states, we consider both χ_{t0} and χ_{t1}. Since they are both P-wave states, their production cross sections are both suppressed by $|R'_P(0)|^2 \propto \alpha_s^5$. For χ_{t0}, we first consider its production via gluon fusion, whose parton-level cross section is given by

$$\hat{\sigma}(gg \to \chi_{t0}) = \frac{12\pi^2\alpha_s^2}{M^3\hat{s}}\,|R'_P(0)\,|^2\delta(\hat{s} - M^2)\ , \tag{3.6}$$

with $M = M_{\chi_{t0}}$, which leads to the proton-level cross section $\sigma(pp \to \chi_{t0}) = 10.0$ fb at the 13-TeV LHC. This result is clearly prevailed by both $\sigma(gg \to \eta_t) = 8.8$ pb and the continuous $\sigma(gg \to t\bar{t}) = 833.9$ pb [62]. On the other hand, $\sigma(f\bar{f} \to \chi_{t0}) \propto m_f^2$ is further suppressed by the small fermion masses both at the LHC (f being the light quarks) and the lepton colliders (f being the light charged leptons). Therefore, it is unlikely for χ_{t0} to be probed at the LHC and other future colliders.

For χ_{t1}, again, it cannot be produced via gluon fusion due to the Landau-Yang theorem, but since its coupling to a light fermion pair is not suppressed by the fermion mass, one can consider its production at lepton colliders. One starts from the partial width

$$\Gamma(\chi_{t1} \to f\bar{f}) = C_f \frac{96\,\alpha_{\rm EM}^2\,a_t^2}{(M^2 - m_Z^2)^2 c_w^4 s_w^4}\sqrt{1 - \frac{4m_f^2}{M^2}}\left[v_f^2\left(1 + \frac{2m_f^2}{M^2}\right) + a_f^2\left(1 - \frac{4m_f^2}{M^2}\right)\right]|R'_P(0)|^2\ , \tag{3.7}$$

where $M = M_{\chi_{t1}}$, $C_f = 1, 3$ is the color factor for leptons and quarks, respectively, and

$$v_i = \frac{I_{3L,i}}{2} - Q_i s_w^2, \qquad a_i = \frac{I_{3L,i}}{2}\ , \tag{3.8}$$

with Q_i being the electric charge of the fermion i and $I_{3L} = +1/2$ $(-1/2)$ for up-type quarks and neutrinos (down-type quarks and charged leptons). For $f = e^-$, one can use the B-W formula to obtain $\sigma(e^+e^- \to \chi_{t1}) = 0.54$ fb. Naively estimating with the cross section of the continuous plus ψ_t background $\sigma(e^+e^- \to t\bar{t}/\psi_t) \approx 1.5$ pb (see Figure 6) at $\sqrt{s} = M_{\chi_{t1}}$, one gets a significance of only $\sim 0.56\,\sigma$ with even $\mathcal{L} = 1$ ab^{-1}. Compared to the S-wave ψ_t whose differential cross section $\mathrm{d}\sigma/\mathrm{d}\theta$ is uniformly distributed across the production angle θ of the constituent t after the decay, that of the P-wave χ_{t1} depends non-trivially on θ, and thus one could try to refine the analysis by analyzing the final-state kinematic distributions. However, we do not expect the significance to improve up to $5\,\sigma$ even after performing such analysis. On the other hand, $\sigma(q\bar{q} \to \chi_{t1})$ at the LHC still suffers from the large continuous $t\bar{t}$ background as in the case of χ_{t0}. Therefore, we conclude that it is also unlikely to probe χ_{t1} at the LHC and other future colliders.

4 Toponium as a probe for the real singlet extension

In addition to probing the toponium states themselves, we further consider the prospect of probing BSM physics using the toponium measurement. Here we use the real singlet extension to the SM (SSM) as an example, though one can certainly generalize the framework to other BSM models. For simplicity, we consider the $\mathbb{Z}_2$-symmetric SSM, in which one introduces a $\mathbb{Z}_2$-odd real scalar S. Along with the SM Higgs doublet Φ, the most general renormalizable scalar potential of the SSM is given by

$$V(\Phi, S) = -\mu^2 \Phi^\dagger \Phi - m^2 S^2 + \lambda_1 (\Phi^\dagger \Phi)^2 + \lambda_2 S^4 + \lambda_3 S^2 \Phi^\dagger \Phi \ , \tag{4.1}$$

where we follow the coupling normalization convention of Ref. [97]. Parameterizing the fields as $\Phi = (0, \frac{h_1+v}{\sqrt{2}})^T$ and $S = \frac{h_2+x}{\sqrt{2}}$, where v and x denote the vacuum expectation values (VEVs) of the fields, respectively, one obtains the minimization conditions

$$m^2 = \lambda_1 v^2 + \frac{\lambda_3}{2} x^2, \qquad \mu^2 = \lambda_2 x^2 + \frac{\lambda_3}{2} v^2 \ , \tag{4.2}$$

which lead to the mass matrix in the $(h_1, h_2)^T$ basis as

$$M^2 = \begin{pmatrix} 2\,\lambda_1\, v^2 & \lambda_3\, v\, x \\ \lambda_3\, v\, x & 2\,\lambda_2\, x^2 \end{pmatrix} \ . \tag{4.3}$$

Denoting α as the mixing angle between $h_{1,2}$, one gets the mixing matrix

$$\begin{pmatrix} \phi \\ H \end{pmatrix} = \begin{pmatrix} \cos\alpha & \sin\alpha \\ -\sin\alpha & \cos\alpha \end{pmatrix} \begin{pmatrix} h_1 \\ h_2 \end{pmatrix} \ , \tag{4.4}$$

where we identify H with the 125-GeV Higgs boson observed at the LHC and ϕ with the exotic mass eigenstate with $m_\phi < m_H = 125$ GeV. Under this mixing convention, the SM Higgs is recovered at the decoupling limit $\sin\alpha = -1$. Consequently, one can write down the top Yukawa interaction in the mass basis as

$$\mathcal{L}_{\rm Yuk} = -\frac{m_t}{v} (\phi \cos\alpha - H \sin\alpha)\, \bar{t}t \ , \tag{4.5}$$

which, in the position space, leads to the Yukawa potential

$$V_{\rm Yuk}(r) = -\frac{1}{4\pi r}\left[\left(\frac{m_t\cos\alpha}{v}\right)^2 e^{-m_\phi r} + \left(\frac{m_t\sin\alpha}{v}\right)^2 e^{-m_H r}\right] . \tag{4.6}$$

As a result, the static potential given in Eq. (2.6) will be modified by the inclusion of the ϕ- and H-mediated Yukawa potentials, which allows us to use the η_t production measurements to indirectly infer the existence of additional scalar fields coupling to the top quark. More specifically, after solving the Schrödinger equation with the modified static potential $V_{\rm static} + V_{\rm Yuk}$, one can obtain the corresponding $E_{\rm bind}$ and $R_S(0)$. These can further be used to predict $\sigma(pp \to \eta_t)$, which can then be compared to the experimental measurements. For simplicity, we only use the results reported in Ref. [62] as a demonstration of the methodology, since, as we will show later, the current precision in η_t measurements is yet high enough to be sensitive to the unexplored parameter space of the SSM. Here, the Yukawa potential mediated by the 125-GeV Higgs boson is suppressed by a factor of $e^{-m_H a_t} \sim \mathcal{O}(10^{-3})$ and thus will not influence the properties of toponium, as already pointed out in Ref. [16]. On the contrary, the light scalar ϕ field could constructively contribute to the static potential (for a color-singlet toponium) and enhance the effective couplings within the toponium system with great significance. Consequently, the experimental measurements will exclude the parameter space where $\cos\alpha \gtrsim 0$ (or where $|\sin\alpha| \lesssim 1$), as we will show later.

On the other hand, the current Higgs exotic decay can also be used to constrain this model. Denoting $\tan\beta \equiv v/x$, the width of the decay channel $H \to \phi\phi$ for $m_\phi < m_H/2$ is given by [97]

$$\Gamma(H \to \phi\phi) = \frac{1}{8\pi m_H}\sqrt{1-\frac{4m_\phi^2}{m_H^2}}\left[\frac{\sin 2\alpha}{2v}(\tan\beta\sin\alpha + \cos\alpha)\left(m_\phi^2 + \frac{m_H^2}{2}\right)\right]^2 . \tag{4.7}$$

We show the 95% CL constraint on BR($H \to \phi\phi$) on the ($\sin\alpha$)–($\tan\beta$) plane obtained from Ref. [68, 98] for four benchmark masses $m_\phi = 0, 1, 10, 30$ GeV in Figure 8. The 95% CL constraints with regard to the Yukawa potential variation derived from the η_t measurement are also presented in Figure 8, from which one can see that for all four benchmark masses, the allowed parameter space by the BR($H \to \phi\phi$) constraint, which roughly follows the $\tan\beta\sin\alpha + \cos\alpha = 0$ contour that gives BR($H \to \phi\phi$) = 0, is further ruled out by the η_t production measurement down to the region around $(\sin\alpha, \tan\beta) = (-1, 0)$. Since the top Yukawa coupling of the 125-GeV Higgs boson is also modified to $y_t = -m_t\sin\alpha/v$ [see Eq. (4.5)], we show in Figure 8 the preferred ranges of $\sin\alpha$ by two types of top Yukawa coupling measurements (see Ref. [88] for a review): the direct measurement of $t\bar{t}H$ production cross section gives $y_t = 0.95^{+0.07}_{-0.08}$ [100, 101], while the measurement of the loop-induced correction to the kinematic distribution of the $t\bar{t}$ final state, which mainly comes from the top Yukawa coupling between t and $\bar{t}$, gives $y_t = 1.16^{+0.24}_{-0.35}$ [99]. It can be seen that the exclusion by the η_t measurement has not yet reached the current limits imposed by the top Yukawa coupling measurements. However, as future measurements of η_t are expected to improve further, they could potentially exclude a larger region of the parameter space. Finally, while we only present the study on the SSM as an example, one can certainly generalize this framework to other BSM models that afford a more sophisticated top Yukawa coupling structure, for which the η_t measurement may impose a more non-trivial constraint.

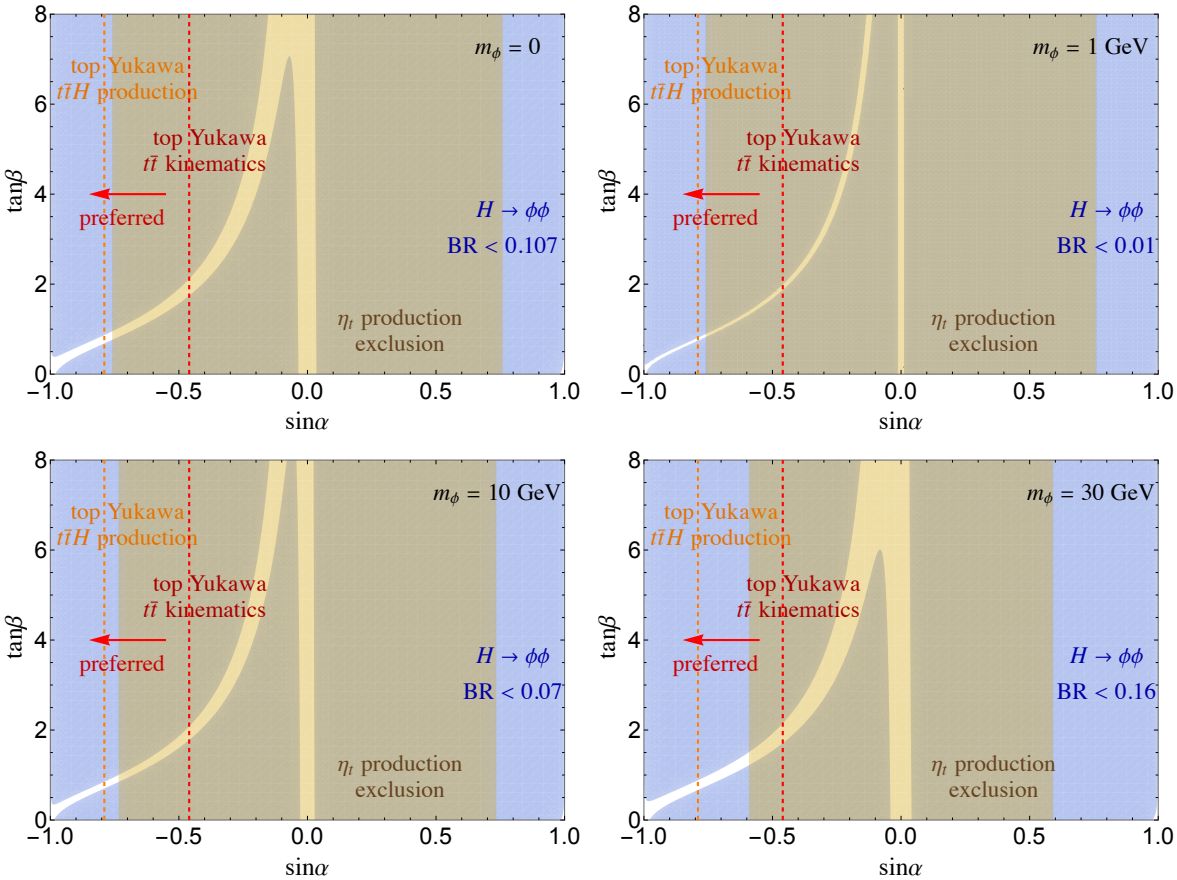

Figure 8: The 95% CL constraint on BR($H \to \phi\phi$) obtained from Refs. [68, 98] (blue) and that imposed by the η_t production measurement performed in Ref. [62] (brown) on the ($\sin\alpha$)–($\tan\beta$) plane for four benchmark masses $m_\phi = 0, 1, 10, 30$ GeV. We also show the preferred regions (red arrow) by the 125-GeV Higgs top Yukawa coupling measurements at 95% CL summarized in Ref. [88] with two dashed lines: the red one is measured through the $t\bar{t}$ kinematics [99] and the orange one through the $t\bar{t}H$ production cross section [100, 101].

5 Discussion and conclusions

We remark again that, as we have discussed and demonstrated in Section 3.1 through Figure 3, the theoretical predictions of toponium properties performed in Refs. [62, 63] still suffer from the uncertainty arising from M_{η_t}. Therefore, it is important to revisit the analysis to pin down the production cross section $\sigma(pp \to \eta_t)$ in a more rigorous manner, which, along with the measured toponium mass, could provide a measure for the top quark mass and width (see Ref. [88] for a review of the existing top quark mass measurements). Since η_t and ψ_t have approximately the same mass, a precise measurement of the η_t mass at the HL-LHC can help determine the center-of-mass energy around the $t\bar{t}$ threshold to be scanned at FCC-ee (see Ref. [85] for the N^{3}LO QCD calculation and Ref. [41] for projected measurements of the top quark mass and width near the $t\bar{t}$ threshold region at a future lepton collider).

Besides the projection and Green function methods, one can also use the "bound state effective field theory (BSEFT)" to study toponium decays and production, such as introduced in

Ref. [52]. However, since the effective couplings in the BSEFT are derived under the assumption that all participant particles are on-shell, it can only be used to study the processes in which the fields interacting with the toponium are all external. For example, the $\psi_t b\bar{b}$ vertex derived from the BSEFT is given by $\bar{b}\gamma_\mu(g^V_{\psi_t b} - g^A_{\psi_t b}\gamma^5)b\psi_t^\mu$, where

$$g^V_{\psi_t b} = \sqrt{\frac{(C_F\alpha_s)^3\pi}{3}}\frac{\alpha_{\rm EM}}{12}\left\{\frac{m_t^2}{s_w^2}\left[\frac{4(8c_w^2+1)s_w^2-9}{c_w^2(Q^2-m_Z^2)}+\frac{3(2-K^2/m_W^2)}{K^2-m_W^2}\right]-8\frac{4m_t^2}{Q^2}\right\}\ , \tag{5.1}$$

$$g^A_{\psi_t b} = -\sqrt{\frac{(C_F\alpha_s)^3\pi}{3}}\frac{\alpha_{\rm EM}\,m_t^2}{4s_w^2}\left[\frac{3-8s_w^2}{c_w^2(Q^2-m_Z^2)}-\frac{2-K^2/m_W^2}{K^2-m_W^2}\right]\ , \tag{5.2}$$

with $k_{1,2}$ denoting the outgoing momenta of b and $\bar{b}$, respectively, and, for simplicity, $Q^2 \equiv (k_1+k_2)^2 = M^2_{\psi_t}$ and $K^2 \equiv (k_1-k_2)^2/4 = -M^2_{\psi_t}/4$ in the $m_b \to 0$ limit. However, in the general case where b and $\bar{b}$ are not necessarily on-shell, not only will Q^2 and K^2 depend on the exact kinematics of the scattering process, but there will also be an additional term $\propto K^\mu$ that can only be captured by the projection method. We have checked that this discrepancy will lead to a huge difference in the predicted production cross section of the $pp \to \psi_t b\bar{b}$ process, which is also the case for other interactions and corresponding production mechanisms. Therefore, one should be careful about using the BSEFT to study toponium phenomenology.

In addition to the physics discussed in the main text, one might also consider probing CP-violation in the top Yukawa coupling via the annihilation decay modes of toponia that involve H. For instance, in the presence of CP-violation, the $\psi_t \to \gamma H$ decay width [see Eq. (A.13) for the corresponding formula] will scale from $|y_t^2| \to |y_t|^2 + |y_t'|^2$, y_t and y_t' denoting the possible CP-even and CP-odd components of top Yukawa coupling, respectively, while some originally forbidden decay modes such as $\eta_t \to HH$ will be turned on. Although these effects are difficult to be measured and tightly constrained by the experimental measurements to date, it still remains an interesting question whether one can use these toponium decays to probe certain BSM physics that introduces CP-violation.

Another important implication of toponium physics is the effect of ψ_t on the electroweak precision tests, which has been studied in Ref. [102]. Denoting the Fermi constant as G_F and using the Green function method, one can show that [5]

$$\Delta\rho(\mu) = \frac{G_F}{8\sqrt{2}}N_c C_F\frac{\alpha_s(\mu)}{\pi}m_t E_{\rm bind}\ , \tag{5.3}$$

$$\Delta r(\mu) = -\frac{c_w^2}{s_w^2}\Delta\rho(\mu)\left[1-\left(1-\frac{8}{3}s_w^2\right)^2\frac{m_Z^2}{(2m_t)^2-m_Z^2}\right]-\frac{N_c\,C_F\,\alpha_{\rm EM}\,\alpha_s(\mu)E_{\rm bind}}{9\,m_t}\ , \tag{5.4}$$

which, after plugged into

$$m_W^2 = \frac{m_Z^2}{2}\left\{1+\sqrt{1-\frac{4\pi\,\alpha_{\rm EM}}{\sqrt{2}\,G_F\,m_Z^2}\left[1+\Delta r(m_W)\right]}\right\}\ , \tag{5.5}$$

along with $E_{\rm bind} = -2.725$ GeV, gives $\Delta m_W \approx -4.0$ MeV, which is comparable to the state-of-the-art measurement uncertainty (≈ 10 MeV) performed by CMS [104]. While of course one

[5] We are not aware that the public `HEPfit` package [103] for global electroweak precision observable fits has implemented this correction.

needs to further consider other sources of corrections, as one of the main objectives of FCC-ee is an even more precise test on the electroweak theory, a more comprehensive understanding of threshold $t\bar{t}$ and ψ_t effects is crucial to the interpretation of future experiments.

In conclusion, we have calculated some theoretical properties of toponia, including their masses, decays, and production at colliders. To study their annihilation decay modes and production mechanisms, we have adopted both projection and Green function methods and found that they both gave comparable results to the CMS measurement of the $pp \to \eta_t$ production cross section at the 13-TeV LHC. Using the projection method, we have studied the sensitivity of the four lowest-lying toponium states at the current LHC and future HL-LHC and FCC-ee, where we have found that η_t is likely to be probed via the associated production of $\eta_t b\bar{b}$ at the hadron colliders and ψ_t at the lepton colliders, while the other two P-wave states, χ_{t0} and χ_{t1}, seem unlikely to be probed in the near future. Finally, we have also used the SSM as an example to show how one can constrain the parameter space of BSM models with the η_t measurement.

Acknowledgments

We thank Kaoru Hagiwara, Cheng-Ping Shen and Yu-Jie Zhang for useful discussions. This work is supported by the U.S. Department of Energy under the contract DE-SC-0017647 and DEAC02-06CH11357 at Argonne National Laboratory. TKC is also supported by the Ministry of Education, Taiwan, under the Government Scholarship to Study Abroad.

A Partial width formulas for the annihilation decay modes

In this appendix, we summarize the formulas for the annihilation decay widths of the toponium states adapted from Refs. [3, 42, 71]. We denote $x_X \equiv m_X^2/M^2$, where M is the mass of the corresponding toponium, and define the Källén function $\lambda(a,b,c) \equiv \sqrt{a^2+b^2+c^2-2ab-2bc-2ca}$. For $\psi_t \to b\bar{b}$ and $\chi_{t1} \to b\bar{b}$, there is an additional contribution from the W-exchange diagrams compared to the other $f\bar{f}$ decay modes. To turn on this specifically for $f=b$, we define $\delta_{fb}=1$ if $f=b$ and $\delta_{fb}=0$ if otherwise. For simplicity, we set $m_f=0$ in the following expressions.

- η_t (0^{-+}):

$$\Gamma(\eta_t \to W^+W^-) = \frac{3\alpha_{\rm EM}^2}{2M^2 s_w^4 (1-4x_W)^2}\lambda^{3/2}(1,x_W,x_W)|R_S(0)|^2 \ , \tag{A.1}$$

$$\Gamma(\eta_t \to ZZ) = \frac{\alpha_{\rm EM}^2(32s_w^4-24s_w^2+9)^2}{432M^2 s_w^4 c_w^4 (1-2x_Z)^2}\lambda^{3/2}(1,x_Z,x_Z)|R_S(0)|^2 \ , \tag{A.2}$$

$$\Gamma(\eta_t \to ZH) = \frac{3\alpha_{\rm EM}^2}{64M^2 s_w^4 c_w^4 x_Z^2}\lambda^{3/2}(1,x_H,x_Z)|R_S(0)|^2 \ , \tag{A.3}$$

$$\Gamma(\eta_t \to \gamma\gamma) = \frac{64\alpha_{\rm EM}^2}{27M^2}|R_S(0)|^2 \ , \tag{A.4}$$

$$\Gamma(\eta_t \to \gamma Z) = \frac{2\alpha_{\rm EM}^2(3-8s_w^2)^2}{27M^2 s_w^2 c_w^2}\lambda^{1/2}(1,0,x_Z)|R_S(0)|^2 \ , \tag{A.5}$$

$$\Gamma(\eta_t \to gg) = \frac{8\alpha_s^2}{3M^2}|R_S(0)|^2 \ . \tag{A.6}$$

- ψ_t (1^{--}):

$$\Gamma(\psi_t \to f\bar{f}) = \frac{4C_f\alpha_{\rm EM}^2}{M^2}\Bigg\{\left[\frac{2}{3}Q_f + \frac{v_f(1-\frac{8}{3}s_w^2)}{4s_w^2c_w^2(1-x_Z)} - \frac{\delta_{fb}(1+8x_W)}{48s_w^2(1+4x_W)x_W}\right]^2 + \left[\frac{a_f(1-\frac{8}{3}s_w^2)}{4s_w^2c_w^2(1-x_Z)} - \frac{\delta_{fb}(8x_W+1)}{48s_w^2(1+4x_W)x_W}\right]^2\Bigg\}|R_S(0)|^2 \ , \tag{A.7}$$

$$\Gamma(\psi_t \to W^+W^-) = \frac{\alpha_{\rm EM}^2}{64M^2x_W^2s_w^4}\lambda^{3/2}(1,x_W,x_W)\left[\frac{1+20x_W+12x_W^2}{(1-x_Z)^2}\left(1-\frac{16}{3}s_w^2x_Z+\frac{64}{9}s_w^4x_Z^2\right) - \frac{8x_W(5+6x_W)(1-\frac{8}{3}s_w^2x_Z)}{(1-4x_W)(1-x_Z)} + \frac{16x_W(2-x_W)}{(1-4x_W)^2}\right]|R_S(0)|^2 \ , \tag{A.8}$$

$$\Gamma(\psi_t \to ZZ) = \frac{\alpha_{\rm EM}^2(1-\frac{8}{3}s_w^2)^2}{32M^2s_w^4c_w^4(1-2x_Z)^2x_Z}\lambda^{5/2}(1,x_Z,x_Z)|R_S(0)|^2 \ , \tag{A.9}$$

$$\Gamma(\psi_t \to \gamma H) = \frac{4\alpha_{\rm EM}y_t^2}{9\pi M^2}(1-x_H)|R_S(0)|^2 = \frac{2\alpha_{\rm EM}}{9\pi v_{\rm EW}^2}(1-x_H)|R_S(0)|^2 \ , \tag{A.10}$$

$$\Gamma(\psi_t \to ZH) = \frac{\alpha_{\rm EM}^2(1-\frac{8}{3}s_w^2)^2}{32M^2s_w^4c_w^4}\lambda^{1/2}(1,x_H,x_Z) \times \frac{[(1-x_Z)^2-x_H(1-3x_Z)]^2+\frac{1}{2}x_Z[(1-x_Z)^2+x_H(2-x_H)]^2}{x_Z(1-x_Z)^2(1-x_Z-x_H)^2}|R_S(0)|^2 \ , \tag{A.11}$$

$$\Gamma(\psi_t \to \gamma Z) = \frac{2\alpha_{\rm EM}^2(1-x_Z^2)}{9M^2s_w^2c_w^2x_Z}|R_S(0)|^2 \ , \tag{A.12}$$

$$\Gamma(\psi_t \to 3g) = \frac{40(\pi^2-9)\alpha_s^3}{81\pi M^2}|R_S(0)|^2 \ . \tag{A.13}$$

- χ_{t0} (0^{++}):

$$\Gamma(\chi_{t0} \to W^+W^-) = \frac{3\alpha_{\rm EM}^2}{4M^4s_w^4x_W^2}\lambda^{1/2}(1,x_W,x_W)\Bigg\{\left[\frac{2(1-x_W)}{1-4x_W} - \frac{3(1-2x_W)}{2(1-x_H)}\right]^2 + 2x_W^2\left[\frac{2}{1-4x_W}+\frac{3}{1-x_H}\right]^2\Bigg\}|R_P'(0)|^2 \ , \tag{A.14}$$

$$\Gamma(\chi_{t0} \to ZZ) = \frac{96\alpha_{\rm EM}^2}{M^4s_w^4c_w^4x_Z^2}\lambda^{1/2}(1,x_Z,x_Z)\Bigg\{\left[\frac{(1-\frac{8}{3}s_w^2)^2x_Z^2}{8(1-2x_Z)^2} - \frac{1}{16} + \frac{3}{32}\frac{1-2x_Z}{1-x_H}\right]^2 + \frac{1}{2}x_Z^2\left[\frac{-(1-\frac{8}{3}s_w^2)^2(3-8x_Z)+(3-4x_Z)}{16(1-2x_Z)} - \frac{3}{8(1-x_H)}\right]^2\Bigg\}|R_P'(0)|^2 \ , \tag{A.15}$$

$$\Gamma(\chi_{t0} \to HH) = \frac{3\alpha_{\rm EM}^2}{32M^4 s_w^4 x_W^2}\lambda^{1/2}(1, x_H, x_H)\left[\frac{5-8x_H}{(1-2x_H)^2} - \frac{9x_H}{1-x_H}\right]^2 |R'_P(0)|^2 \ , \tag{A.16}$$

$$\Gamma(\chi_{t0} \to \gamma\gamma) = \frac{256\alpha_{\rm EM}^2}{3M^4}|R'_P(0)|^2 \ , \tag{A.17}$$

$$\Gamma(\chi_{t0} \to Z\gamma) = \frac{24\alpha_{\rm EM}^2}{M^4 s_w^2 c_w^2}\left(1 - \frac{8}{3}s_w^2\right)^2 \frac{(1-\frac{1}{3}x_Z)^2}{1-x_Z}|R'_P(0)|^2 \ , \tag{A.18}$$

$$\Gamma(\chi_{t0} \to gg) = \frac{96\alpha_s^2}{M^4}|R'_P(0)|^2 \ . \tag{A.19}$$

- χ_{t1} (1^{++}):

$$\Gamma(\chi_{t1} \to f\bar{f}) = \frac{96C_f\alpha_{\rm EM}^2}{M^4}\Bigg\{\left[\frac{a_f}{4s_w^2c_w^2(1-x_Z)} - \frac{\delta_{fb}(-1+8x_W)}{48s_w^2(1+4x_W)x_W}\right]^2 + \left[\frac{v_f}{4s_w^2c_w^2(1-x_Z)} - \frac{\delta_{fb}(-1+8x_W)}{48s_w^2(1+4x_W)x_W}\right]^2\Bigg\}|R'_P(0)|^2 \ , \tag{A.20}$$

$$\Gamma(\chi_{t1} \to W^+W^-) = \frac{3\alpha_{\rm EM}^2}{2M^4 s_w^4 x_W(1-4x_W)^2}\lambda^{3/2}(1, x_W, x_W)\Bigg[\frac{64x_W^2}{1-4x_W} + 4\left(\frac{x_Z-4x_W}{1-x_Z}\right)^2 + \frac{(1+4x_W-2x_Z)^2(1+4x_W+12x_W^2)}{4x_W(1-x_Z)^2}\Bigg]|R'_P(0)|^2 \ , \tag{A.21}$$

$$\Gamma(\chi_{t1} \to ZZ) = \frac{3\alpha_{\rm EM}^2}{16M^4 s_w^4 c_w^4 x_Z(1-2x_Z)^2}\lambda^{5/2}(1, x_Z, x_Z)\left[1 - \frac{2(1-\frac{8}{3}s_w^2)^2 x_Z}{1-2x_Z}\right]^2 |R'_P(0)|^2 \ , \tag{A.22}$$

$$\Gamma(\chi_{t1} \to ZH) = \frac{3\alpha_{\rm EM}^2}{8s_w^4c_w^4M^4x_Z^2(1-x_Z-x_H)^2}\lambda^{1/2}(1, x_Z, x_H) \times \Bigg\{(1+x_Z-x_H)^2\left(1-x_Z+\frac{x_Hx_Z}{1-x_Z}\right)^2 + \frac{1}{2}x_Z \times \left[3-3x_Z+x_H+4x_Hx_Z\left(\frac{1}{1-x_Z}+\frac{1}{1-x_Z-x_H}\right)\right]^2\Bigg\}|R'_P(0)|^2 \ , \tag{A.23}$$

$$\Gamma(\chi_{t1} \to \gamma Z) = \frac{16\alpha_{\rm EM}^2}{3M^4 s_w^2 c_w^2}\left(1 - \frac{8}{3}s_w^2\right)^2 \frac{x_Z(1+x_Z)}{1-x_Z}|R'_P(0)|^2 \ . \tag{A.24}$$

We also list here the cross section formulas for $e^+e^- \to b\bar{b}$ and γZ, including the interference terms with the background processes.

$$\sigma(e^+e^- \to b\bar{b}) = \frac{\sqrt{s-4m_b^2}}{144\pi s^{5/2}s_w^4c_w^4(s-m_Z^2)^2\left[M_{\psi_t}^2(\Gamma_{\psi_t}^2-2s)+M_{\psi_t}^4+s^2\right]} \tag{A.25}$$

$$
\begin{aligned}
&\times \Big\{ -3\pi\alpha_{\rm EM} s c_w^6 s_w^2 \Big[6s(g^A_{\psi_t\ell} - g^V_{\psi_t\ell})(M^2_{\psi_t} - s)(m_Z^2 - s)\big(g^V_{\psi_t b}(2m_b^2 + s) - g^A_{\psi_t b}(s - 4m_b^2)\big) \\
&+ 4\pi\alpha_{\rm EM}(2m_b^2 + s)(2m_Z^2 - s)\big(M^2_{\psi_t}(\Gamma^2_{\psi_t} - 2s) + M^4_{\psi_t} + s^2\big)\Big] \\
&- \pi\alpha_{\rm EM} s c_w^2 s_w^6 \Big[6s(g^A_{\psi_t\ell} + 3g^V_{\psi_t\ell})(M^2_{\psi_t} - s)(s - m_Z^2)\big(3g^A_{\psi_t b}(s - 4m_b^2) + g^V_{\psi_t b}(2m_b^2 + s)\big) \\
&+ 4\pi\alpha_{\rm EM}\big(4m_b^2(3m_Z^2 + 8s) + s(6m_Z^2 - 11s)\big)\big(M^2_{\psi_t}(\Gamma^2_{\psi_t} - 2s) + M^4_{\psi_t} + s^2\big)\Big] \\
&+ 2c_w^2 s_w^4 \Big[18s^2((g^A_{\psi_t\ell})^2 + (g^V_{\psi_t\ell})^2)\left(s - m_Z^2\right)^2 \left((g^A_{\psi_t b})^2(s - 4m_b^2) + (g^V_{\psi_t b})^2(2m_b^2 + s)\right) \\
&- 6\pi\alpha_{\rm EM} s\Big[(M^2_{\psi_t} - s)(m_Z^2 - s)(g^V_{\psi_t b}(2m_b^2 + s)\big(s g^A_{\psi_t\ell} + g^V_{\psi_t\ell}(8m_Z^2 - 3s)\big) - 3s g^A_{\psi_t b}(s - 4m_b^2)(g^A_{\psi_t\ell} + g^V_{\psi_t\ell})\Big] \\
&+ \pi^2\alpha_{\rm EM}^2\Big[m_b^2(-48sm_Z^2 + 64m_Z^4 - 5s^2) + s(-24sm_Z^2 + 32m_Z^4 + 11s^2)\Big]\big(M^2_{\psi_t}(\Gamma^2_{\psi_t} - 2s) + M^4_{\psi_t} + s^2\big)\Big] \\
&- \pi^2\alpha_{\rm EM}^2 s^2\left[5s_w^8(17m_b^2 - 5s) + 9c_w^8(m_b^2 - s)\right]\left[M^2_{\psi_t}(\Gamma^2_{\psi_t} - 2s) + M^4_{\psi_t} + s^2\right]\Big\},
\end{aligned}
$$

where $g^{A,V}_{\psi_t b}$ is defined in Eq. (3.2) and

$$
\begin{aligned}
g^A_{\psi_t\ell} &= -\sqrt{\frac{(C_F\alpha_s)^3\pi}{3}}\,\frac{\alpha_{\rm EM}\, m_t^2(3 - 8s_w^2)}{4s_w^2 c_w^2(4m_t^2 - m_Z^2)}\,, \\
g^V_{\psi_t\ell} &= \sqrt{\frac{(C_F\alpha_s)^3\pi}{3}}\,\frac{\alpha_{\rm EM}[8m_W^2 s_w^2 - 3m_t^2(1 + 4s_w^2)]}{4s_w^2 c_w^2(4m_t^2 - m_Z^2)}\,,
\end{aligned}
\tag{A.26}
$$

are the couplings of ψ_t to leptons defined in $\bar{\ell}\gamma_\mu(g^V_{\psi_t\ell} - g^A_{\psi_t\ell}\gamma^5)\ell\psi_t^\mu$.

$$
\begin{aligned}
&\sigma(e^+e^- \to \gamma Z) = \qquad\qquad (A.27) \\
&\frac{-1}{384\pi s^2 s_w^2 c_w^2 m_Z^2\left(s - m_Z^2\right)\left[(s - M^2_{\psi_t})^2 + M^2_{\psi_t}\Gamma^2_{\psi_t}\right]}\int_{t_{\rm min}}^{t_{\rm max}} {\rm d}t \\
&\Big\{ -8c_w^2 s_w^2 t g^2_{\psi_t ZA}\left[(g^A_{\psi_t\ell})^2 + (g^V_{\psi_t\ell})^2\right]\left(s - m_Z^2\right)\left[-m_Z^2\left(6s^2 + 9st + 4t^2\right) + 3m_Z^4(s + 2t) + s\left(3s^2 + 3st + 2t^2\right)\right] \\
&+ 96\pi\alpha_{\rm EM}\left(4s_w^2 - 1\right)s_w c_w t g_{\psi_t ZA} m_Z^2(g^A_{\psi_t\ell} + g^V_{\psi_t\ell})\left(s - M^2_{\psi_t}\right)\left(s^2 - m_Z^4\right) \\
&+ 96\pi^2\alpha_{\rm EM}^2\left(8s_w^4 - 4s_w^2 + 1\right)m_Z^2\left[(s - M^2_{\psi_t})^2 + M^2_{\psi_t}\Gamma^2_{\psi_t}\right]\left[(m_Z^4 + s^2)\log\left(\frac{t}{-m_Z^2 + s + t}\right) + 2t(s - m_Z^2)\right]\Big\},
\end{aligned}
$$

where $g_{\psi_t ZA}$ is defined in Eq. (3.5) and $t_{\rm min}$ and $t_{\rm max}$ are determined by the kinematic cuts for IR regularization on the photon. In terms of the maximum scattering angle θ_m with respect to the collision axis, $t_{\rm min/max} = -(s - m_Z^2)(1 \mp \cos\theta_m)$.

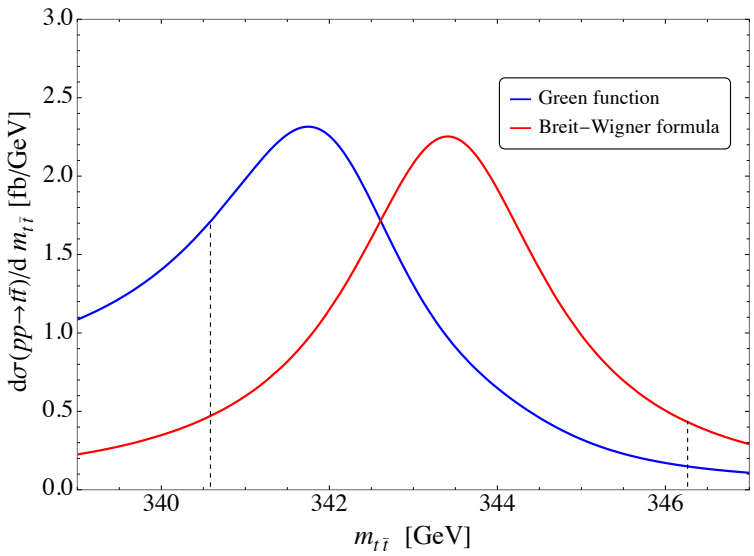

Figure 9: The $d\sigma(pp \to \chi_{t0})/dm_{t\bar{t}}$ distributions at the 13-TeV LHC calculated from the leading-order Green function method and B-W formula. The two dashed lines represent $m_{t\bar{t}} = M_{\chi_{t0}} \pm \Gamma$ with $M_{\chi_{t0}} = 343.43$ GeV and $\Gamma = 2.84$ GeV, respectively, between which we identify the $t\bar{t}$ system to be on "resonance".

B Green function method for P-wave states

In this appendix, we compare the Green function and projection methods for P-wave toponium states. Following Ref. [105], one can write down

$$\sigma(gg \to t\bar{t} \to bW^+\bar{b}W^-)_P = \sigma(gg \to t\bar{t} \to bW^+\bar{b}W^-)_{P,\text{tree}} \frac{\text{Im}[\nabla^2 G(r,E)]_{r=0}}{\text{Im}[\nabla^2 G_0(r,E)]_{r=0}} \,, \tag{B.1}$$

where, approximating the static potential with V_{Coul} and using Eq. (2.21), one has

$$\mathcal{S}_P(E) \equiv \frac{\text{Im}[\nabla^2 G(r,E)]_{r=0}}{\text{Im}[\nabla^2 G_0(r,E)]_{r=0}} = \frac{\text{Im}\left[-a^2 \log\left(-2i\sqrt{z'}\right) - a^2\,\psi^{(0)}\left(1 - i\frac{a}{2\sqrt{z'}}\right) + ia\sqrt{z'} + z'\right]}{\text{Im}\left[z'\right]} \,. \tag{B.2}$$

Using the χ_{t0} state for example, its parton-level production cross section $\hat{\sigma}(gg \to t\bar{t})_{^3P_0,\text{tree}}$ near the threshold is given by

$$\hat{\sigma}(gg \to t\bar{t})_{^3P_0,\text{tree}} = \frac{\pi\,\alpha_s^2\,(24m_t^2 + \hat{s})}{144\,\hat{s}\,(2m_t + \sqrt{\hat{s}})^2}\left(1 - \frac{4m_t^2}{\hat{s}}\right)^{\frac{3}{2}} \,, \tag{B.3}$$

where we have simply assumed $M = 2m_t$. We show the corresponding proton-level differential cross section $d\sigma(pp \to t\bar{t})/dm_{t\bar{t}}$ derived from the Green function as well as the B-W formula in Figure 9. By integrating over the "resonance" interval $m_{t\bar{t}} \in [M_{\chi_{t0}} - \Gamma, M_{\chi_{t0}} + \Gamma] = [343.43 - 2.84, 343.43 + 2.84]$ GeV, one gets the cross section of $\sigma(pp \to \chi_{t0})_{\text{Green}} = 6.61$ fb, which is compatible with $\sigma(pp \to \chi_{t0})_{\text{Projection}} = 10.0$ fb obtained through the projection method. Note

that there is a displacement between the locations of the resonance peak predicted by the two methods, which could be due to the incomplete treatment of the P-wave Green function method adopted thus far. As demonstrated in Ref. [106], the peak location of the P-wave spectrum predicted by the Green function method depends heavily on the relative velocity (and thus momentum) between the constituents t and $\bar{t}$, while that of the S-wave spectrum is less sensitive, as can be seen from the results in Ref. [107]. Therefore, it is perhaps more favorable to formulate the P-wave Green function method in the momentum space, as has been proposed in Refs. [15, 56] and carried out for the S-wave states in Ref. [13]. On top of this, Ref. [105] further points out that higher-order corrections to the P-wave Green function will induce a divergent term absent from the S-wave Green function, which, so far, cannot be dealt with using the known methods in the literature. As a result, it still remains to be explored the exact differential cross section predicted by the P-wave Green function method.

References

[1] R. J. Eden, P. V. Landshoff, D. I. Olive and J. C. Polkinghorne, *The analytic S-matrix*. Cambridge Univ. Press, Cambridge, 1966.

[2] I. I. Y. Bigi, Y. L. Dokshitzer, V. A. Khoze, J. H. Kuhn and P. M. Zerwas, *Production and Decay Properties of Ultraheavy Quarks*, *Phys. Lett. B* **181** (1986) 157–163.

[3] V. D. Barger, E. W. N. Glover, K. Hikasa, W.-Y. Keung, M. G. Olsson, C. J. Suchyta, III et al., *Superheavy Quarkonium Production and Decays: A New Higgs Signal*, *Phys. Rev. D* **35** (1987) 3366.

[4] N. Fabiano, A. Grau and G. Pancheri, *Observability limits for toponium at hadron colliders*, *Phys. Rev. D* **50** (1994) 3173–3175.

[5] Y. Kiyo, J. H. Kuhn, S. Moch, M. Steinhauser and P. Uwer, *Top-quark pair production near threshold at LHC*, *Eur. Phys. J. C* **60** (2009) 375–386, [0812.0919].

[6] K. Hagiwara, Y. Sumino and H. Yokoya, *Bound-state Effects on Top Quark Production at Hadron Colliders*, *Phys. Lett. B* **666** (2008) 71–76, [0804.1014].

[7] Y. Kats and M. D. Schwartz, *Annihilation decays of bound states at the LHC*, *JHEP* **04** (2010) 016, [0912.0526].

[8] Y. Sumino and H. Yokoya, *Bound-state effects on kinematical distributions of top quarks at hadron colliders*, *JHEP* **09** (2010) 034, [1007.0075].

[9] J. H. Kühn, A. Scharf and P. Uwer, *Weak Interactions in Top-Quark Pair Production at Hadron Colliders: An Update*, *Phys. Rev. D* **91** (2015) 014020, [1305.5773].

[10] B. Fuks, K. Hagiwara, K. Ma and Y.-J. Zheng, *Signatures of toponium formation in LHC run 2 data*, *Phys. Rev. D* **104** (2021) 034023, [2102.11281].

[11] J. A. Aguilar-Saavedra, *Toponium hunter's guide*, *Phys. Rev. D* **110** (2024) 054032, [2407.20330].

[12] M. V. Garzelli, G. Limatola, S. O. Moch, M. Steinhauser and O. Zenaiev, *Updated predictions for toponium production at the LHC*, *Phys. Lett. B* **866** (2025) 139532, [2412.16685].

[13] B. Fuks, K. Hagiwara, K. Ma and Y.-J. Zheng, *Simulating toponium formation signals at the LHC*, *Eur. Phys. J. C* **85** (2025) 157, [2411.18962].

[14] B. Fuks, *Toponium physics at the Large Hadron Collider*, May, 2025, 2505.03869.

[15] V. S. Fadin and V. A. Khoze, *Threshold Behavior of Heavy Top Production in e+ e- Collisions*, *JETP Lett.* **46** (1987) 525–529.

[16] M. J. Strassler and M. E. Peskin, *The Heavy top quark threshold: QCD and the Higgs*, *Phys. Rev. D* **43** (1991) 1500–1514.

[17] W. Beenakker and W. Hollik, *Higgs boson effects in e+ e- —> t anti-t close to the threshold*, *Phys. Lett. B* **269** (1991) 425–431.

[18] Y. Sumino, K. Fujii, K. Hagiwara, H. Murayama and C. K. Ng, *Top quark pair production near threshold*, *Phys. Rev. D* **47** (1993) 56–81.

[19] H. Murayama and Y. Sumino, *Axial coupling contribution to toponium resonances*, *Phys. Rev. D* **47** (1993) 82–92.

[20] K. Fujii, T. Matsui and Y. Sumino, *Physics at t anti-t threshold in e+ e- collisions*, *Phys. Rev. D* **50** (1994) 4341–4362.

[21] Y. Sumino, *Review on physics of $e^+e^- \to t\bar{t}$ near threshold*, *Acta Phys. Polon. B* **25** (1994) 1837–1856, [hep-ph/9411310].

[22] R. Harlander, M. Jezabek and J. H. Kuhn, *Higgs effects in top quark pair production*, *Acta Phys. Polon. B* **27** (1996) 1781–1788, [hep-ph/9506292].

[23] Y. Sumino, *Top quark pair production and decay near threshold in e+ e- collisions*, *Acta Phys. Polon. B* **28** (1997) 2461–2478, [hep-ph/9711233].

[24] K. Melnikov and A. Yelkhovsky, *Top quark production at threshold with O(alpha-s**2) accuracy*, *Nucl. Phys. B* **528** (1998) 59–72, [hep-ph/9802379].

[25] O. I. Yakovlev, *Top quark production near threshold: NNLO QCD correction*, *Phys. Lett. B* **457** (1999) 170–176, [hep-ph/9808463].

[26] A. A. Penin and A. A. Pivovarov, *Analytical results for e+ e- —> t anti-t and gamma gamma —> t anti-t observables near the threshold up to the next-to-next-to leading order of NRQCD*, *Phys. Atom. Nucl.* **64** (2001) 275–293, [hep-ph/9904278].

[27] T. Nagano, A. Ota and Y. Sumino, *O(alpha(s)**2) corrections to e+ e- —> t anti-t total and differential cross-sections near threshold*, *Phys. Rev. D* **60** (1999) 114014, [hep-ph/9903498].

[28] J. H. Kuhn and T. Teubner, *Axial contributions at the top threshold*, *Eur. Phys. J. C* **9** (1999) 221–228, [hep-ph/9903322].

[29] M. Beneke, A. Signer and V. A. Smirnov, *Top quark production near threshold and the top quark mass*, *Phys. Lett. B* **454** (1999) 137–146, [hep-ph/9903260].

[30] A. H. Hoang and T. Teubner, *Top quark pair production close to threshold: Top mass, width and momentum distribution*, *Phys. Rev. D* **60** (1999) 114027, [hep-ph/9904468].

[31] A. H. Hoang, A. V. Manohar, I. W. Stewart and T. Teubner, *The Threshold t anti-t cross-section at NNLL order*, *Phys. Rev. D* **65** (2002) 014014, [hep-ph/0107144].

[32] M. Martinez and R. Miquel, *Multiparameter fits to the t anti-t threshold observables at a future e+ e- linear collider*, *Eur. Phys. J. C* **27** (2003) 49–55, [hep-ph/0207315].

[33] D. Eiras and M. Steinhauser, *Complete Higgs mass dependence of top quark pair threshold production to order alpha alpha(s)*, *Nucl. Phys. B* **757** (2006) 197–210, [hep-ph/0605227].

[34] A. H. Hoang, C. J. Reisser and P. Ruiz-Femenia, *Phase Space Matching and Finite Lifetime Effects for Top-Pair Production Close to Threshold*, *Phys. Rev. D* **82** (2010) 014005, [1002.3223].

[35] M. Beneke, B. Jantzen and P. Ruiz-Femenia, *Electroweak non-resonant NLO corrections to e+ e- -> W+ W- b bbar in the t tbar resonance region*, *Nucl. Phys. B* **840** (2010) 186–213, [1004.2188].

[36] A. A. Penin and J. H. Piclum, *Threshold production of unstable top*, *JHEP* **01** (2012) 034, [1110.1970].

[37] M. Beneke, Y. Kiyo and K. Schuller, *Third-order correction to top-quark pair production near threshold. Part I. Effective theory set-up and matching coefficients*, *JHEP* **07** (2025) 273, [1312.4791].

[38] M. Beneke, A. Maier, J. Piclum and T. Rauh, *Higgs effects in top anti-top production near threshold in e^+e^- annihilation*, *Nucl. Phys. B* **899** (2015) 180–193, [1506.06865].

[39] F. Bach, B. C. Nejad, A. Hoang, W. Kilian, J. Reuter, M. Stahlhofen et al., *Fully-differential Top-Pair Production at a Lepton Collider: From Threshold to Continuum*, *JHEP* **03** (2018) 184, [1712.02220].

[40] J.-H. Fu, Y.-J. Li, H.-M. Yang, Y.-B. Li, Y.-J. Zhang and C.-P. Shen, *Toponium: the smallest bound state and simplest hadron in quantum mechanics*, 2412.11254.

[41] M. M. Defranchis, J. de Blas, A. Mehta, M. Selvaggi and M. Vos, *A detailed study on the prospects for a $\mathrm{t\bar{t}}$ threshold scan in $\mathrm{e^+e^-}$ collisions*, 2503.18713.

[42] J. H. Kuhn and P. M. Zerwas, *The Toponium Scenario*, *Phys. Rept.* **167** (1988) 321.

[43] Y. Yang, B. Yang, J. Li, Z. Lu and J. Sun, *Searching for the toponium η_t with the $\eta_t \to W^+W^-$ decay*, *Chin. Phys. C* **50** (2026) 033101, [2410.22841].

[44] R. Francener, V. P. Goncalves and D. E. Martins, *Investigating the exclusive toponium production at the LHC and FCC*, *Phys. Rev. D* **112** (2025) 094050, [2502.03295].

[45] W. Kummer and W. Modritsch, *Rigorous QCD potential for the t anti-t system at threshold*, *Z. Phys. C* **66** (1995) 225–240, [hep-ph/9408216].

[46] N. Fabiano, G. Pancheri and A. Grau, *Toponium from different potential models*, *Nuovo Cim. A* **107** (1994) 2789–2804.

[47] T. Kawanai and S. Sasaki, *Heavy quarkonium potential from Bethe-Salpeter wave function on the lattice*, *Phys. Rev. D* **89** (2014) 054507, [1311.1253].

[48] N. Akbar, I. Asghar and Z. Ahmad, *Properties of Toponium Mesons with Non-relativistic QCD Potential Model*, 2411.08548.

[49] G.-L. Wang, T.-F. Feng and Y.-Q. Wang, *Mass spectra and wave functions of toponia*, *Phys. Rev. D* **111** (2025) 096016, [2411.17955].

[50] S.-J. Jiang, B.-Q. Li, G.-Z. Xu and K.-Y. Liu, *Study on Toponium: Spectrum and Associated Processes*, 2412.18527.

[51] M. Beneke, P. Falgari, S. Klein and C. Schwinn, *Hadronic top-quark pair production with*

NNLL threshold resummation, *Nucl. Phys. B* **855** (2012) 695–741, [1109.1536].

[52] J.-H. Fu, Y.-J. Zhang, G.-Z. Xu and K.-Y. Liu, *Toponium: Implementation of a toponium model in FeynRules*, 2504.12634.

[53] A. Djouadi, J. Ellis and J. Quevillon, *Contrasting pseudoscalar Higgs and toponium states at the LHC and beyond*, *Phys. Lett. B* **866** (2025) 139583, [2412.15138].

[54] C.-T. Lu, K. Cheung, D. Kim, S. Lee and J. Song, *Can a pseudoscalar with a mass of 365 GeV in two-Higgs-doublet models explain the CMS tt^{-} excess?*, *Phys. Lett. B* **859** (2024) 139121, [2410.08609].

[55] F. J. Llanes-Estrada, *Ensuring that toponium is glued, not nailed*, *Phys. Lett. B* **866** (2025) 139510, [2411.19180].

[56] V. S. Fadin, V. A. Khoze and M. I. Kotsky, *Top quark polarization as a probe of t anti-t threshold dynamics*, *Z. Phys. C* **64** (1994) 45–56, [hep-ph/9403246].

[57] M. Jezabek, J. H. Kuhn, M. Peter, Y. Sumino and T. Teubner, *The Perturbative QCD potential and the t anti-t threshold*, *Phys. Rev. D* **58** (1998) 014006, [hep-ph/9802373].

[58] F. Maltoni, C. Severi, S. Tentori and E. Vryonidou, *Quantum tops at circular lepton colliders*, *JHEP* **09** (2024) 001, [2404.08049].

[59] J. A. Aguilar-Saavedra and J. A. Casas, *Entanglement Autodistillation from Particle Decays*, *Phys. Rev. Lett.* **133** (2024) 111801, [2401.06854].

[60] T. Han, M. Low, N. McGinnis and S. Su, *Measuring quantum discord at the LHC*, *JHEP* **05** (2025) 081, [2412.21158].

[61] P. Nason, E. Re and L. Rottoli, *Spin Correlations in $t\bar{t}$ Production and Decay at the LHC in QCD Perturbation Theory*, 2505.00096.

[62] CMS collaboration, A. Hayrapetyan et al., *Observation of a pseudoscalar excess at the top quark pair production threshold*, *Rept. Prog. Phys.* **88** (2025) 087801, [2503.22382].

[63] ATLAS collaboration, G. Aad et al., *Observation of a cross-section enhancement near the $t\bar{t}$ production threshold in $\sqrt{s} = 13$ TeV pp collisions with the ATLAS detector*, 2601.11780.

[64] M. Peter, *The Static quark - anti-quark potential in QCD to three loops*, *Phys. Rev. Lett.* **78** (1997) 602–605, [hep-ph/9610209].

[65] M. Peter, *The Static potential in QCD: A Full two loop calculation*, *Nucl. Phys. B* **501** (1997) 471–494, [hep-ph/9702245].

[66] Y. Schroder, *The Static potential in QCD to two loops*, *Phys. Lett. B* **447** (1999) 321–326, [hep-ph/9812205].

[67] A. Vairo, *The QCD potential*, *AIP Conf. Proc.* **964** (2007) 102–109, [0709.3341].

[68] Particle Data Group collaboration, S. Navas et al., *Review of particle physics*, *Phys. Rev. D* **110** (2024) 030001.

[69] V. D. Barger and W.-Y. Keung, *Higgs Boson Production via Pseudoscalar Toponium*, *Phys. Rev. D* **37** (1988) 3172–3175.

[70] J. Feigenbaum, *Study of toponium production including the effects of Higgs exchange*, *Phys. Rev. D* **43** (1991) 264–267.

[71] J. H. Kuhn, *Weak Interactions of Quarkonia*, *Acta Phys. Polon. B* **12** (1981) 347.

[72] A. H. Hoang et al., *Top - anti-top pair production close to threshold: Synopsis of recent NNLO results*, *Eur. Phys. J. direct* **2** (2000) 3, [hep-ph/0001286].

[73] L. D. Landau, *On the angular momentum of a system of two photons*, *Dokl. Akad. Nauk SSSR* **60** (1948) 207–209.

[74] C.-N. Yang, *Selection Rules for the Dematerialization of a Particle Into Two Photons*, *Phys. Rev.* **77** (1950) 242–245.

[75] K. Agashe et al., *Report of the Topical Group on Top quark physics and heavy flavor production for Snowmass 2021*, 2209.11267.

[76] FCC collaboration, M. Benedikt et al., *Future Circular Collider Feasibility Study Report: Volume 1, Physics, Experiments, Detectors*, 2505.00272.

[77] FCC collaboration, M. Benedikt et al., *Future Circular Collider Feasibility Study Report: Volume 2, Accelerators, Technical Infrastructure and Safety*, 2505.00274.

[78] The European Strategy Group (ESG), *The European Strategy for Particle Physics: 2026 Update - Recommendations by the European Strategy Group*, 12, 2025, doi:10.17181/CERN.423R.S20Z.

[79] Y. Koma, M. Koma and H. Wittig, *Relativistic corrections to the static potential at O(1/m) and O(1/m**2)*, *PoS* **LATTICE2007** (2007) 111, [0711.2322].

[80] T. Barnes, S. Godfrey and E. S. Swanson, *Higher charmonia*, *Phys. Rev. D* **72** (2005) 054026, [hep-ph/0505002].

[81] Y. Bai and S. Westhoff, *Darkonia at colliders*, *JHEP* **04** (2025) 042, [2412.03677].

[82] V. S. Fadin, V. A. Khoze and T. Sjostrand, *On the Threshold Behavior of Heavy Top Production*, *Z. Phys. C* **48** (1990) 613–622.

[83] L. Hostler, *Coulomb green's functions and the furry approximation*, *Journal of Mathematical Physics* **5** (05, 1964) 591–611.

[84] J. H. Kuhn and E. Mirkes, *QCD corrections to toponium production at hadron colliders*, *Phys. Rev. D* **48** (1993) 179–189, [hep-ph/9301204].

[85] M. Beneke, Y. Kiyo, P. Marquard, A. Penin, J. Piclum and M. Steinhauser, *Next-to-Next-to-Next-to-Leading Order QCD Prediction for the Top Antitop S-Wave Pair Production Cross Section Near Threshold in e^+e^- Annihilation*, *Phys. Rev. Lett.* **115** (2015) 192001, [1506.06864].

[86] W.-L. Ju, G. Wang, X. Wang, X. Xu, Y. Xu and L. L. Yang, *Top quark pair production near threshold: single/double distributions and mass determination*, *JHEP* **06** (2020) 158, [2004.03088].

[87] CMS collaboration, *Highlights of the HL-LHC physics projections by ATLAS and CMS*, 2504.00672.

[88] CMS collaboration, A. Hayrapetyan et al., *Review of top quark mass measurements in CMS*, *Phys. Rept.* **1115** (2025) 116–218, [2403.01313].

[89] A. D. Martin, W. J. Stirling, R. S. Thorne and G. Watt, *Parton distributions for the LHC*, *Eur. Phys. J. C* **63** (2009) 189–285, [0901.0002].

[90] ATLAS collaboration, G. Aad et al., *Search for heavy resonances decaying into a Z or*

W boson and a Higgs boson in final states with leptons and b-jets in 139 fb^{-1} *of pp collisions at* $\sqrt{s} = 13$ *TeV with the ATLAS detector*, *JHEP* **06** (2023) 016, [2207.00230].

[91] J. Alwall, R. Frederix, S. Frixione, V. Hirschi, F. Maltoni, O. Mattelaer et al., *The automated computation of tree-level and next-to-leading order differential cross sections, and their matching to parton shower simulations*, *JHEP* **07** (2014) 079, [1405.0301].

[92] T. Sjöstrand, S. Ask, J. R. Christiansen, R. Corke, N. Desai, P. Ilten et al., *An introduction to PYTHIA 8.2*, *Comput. Phys. Commun.* **191** (2015) 159–177, [1410.3012].

[93] DELPHES 3 collaboration, J. de Favereau, C. Delaere, P. Demin, A. Giammanco, V. Lemaître, A. Mertens et al., *DELPHES 3, A modular framework for fast simulation of a generic collider experiment*, *JHEP* **02** (2014) 057, [1307.6346].

[94] ATLAS collaboration, *Summary of Diboson Resonance Searches at the ATLAS experiment using full run-2 data*, .

[95] ATLAS collaboration, G. Aad et al., *Measurement of* $t\bar{t}$ *production in association with additional b-jets in the* $e\mu$ *final state in proton–proton collisions at* $\sqrt{s} = 13$ *TeV with the ATLAS detector*, *JHEP* **01** (2025) 068, [2407.13473].

[96] J. Pan, J.-H. Chen, X.-G. He, G. Li and J.-Y. Su, *Triply charged Higgs bosons at a 100 TeV pp collider*, *Eur. Phys. J. C* **81** (2021) 43, [1909.07254].

[97] T. Robens and T. Stefaniak, *Status of the Higgs Singlet Extension of the Standard Model after LHC Run 1*, *Eur. Phys. J. C* **75** (2015) 104, [1501.02234].

[98] M. Carena, J. Kozaczuk, Z. Liu, T. Ou, M. J. Ramsey-Musolf, J. Shelton et al., *Probing the Electroweak Phase Transition with Exotic Higgs Decays*, *LHEP* **2023** (2023) 432, [2203.08206].

[99] CMS collaboration, A. M. Sirunyan et al., *Measurement of the top quark Yukawa coupling from* $\mathrm{t\bar{t}}$ *kinematic distributions in the dilepton final state in proton-proton collisions at* $\sqrt{s} = 13$ *TeV*, *Phys. Rev. D* **102** (2020) 092013, [2009.07123].

[100] ATLAS collaboration, G. Aad et al., *A detailed map of Higgs boson interactions by the ATLAS experiment ten years after the discovery*, *Nature* **607** (2022) 52–59, [2207.00092].

[101] CMS collaboration, A. Tumasyan et al., *A portrait of the Higgs boson by the CMS experiment ten years after the discovery.*, *Nature* **607** (2022) 60–68, [2207.00043].

[102] B. A. Kniehl and A. Sirlin, *On the effect of the* $t\bar{t}$ *threshold on electroweak parameters*, *Phys. Rev. D* **47** (1993) 883–893.

[103] J. De Blas et al., ***HEPfit**: a code for the combination of indirect and direct constraints on high energy physics models*, *Eur. Phys. J. C* **80** (2020) 456, [1910.14012].

[104] CMS collaboration, V. Chekhovsky et al., *High-precision measurement of the W boson mass with the CMS experiment at the LHC*, 2412.13872.

[105] C. H. de Lima, A. Tonero, A. Vasquez and R. Rosenfeld, *P-wave Sommerfeld enhancement near threshold: a simplified approach*, *Eur. Phys. J. C* **83** (2023) 939, [2208.13309].

[106] R. Iengo, *Sommerfeld enhancement: General results from field theory diagrams*, *JHEP*

05 (2009) 024, [0902.0688].

[107] M. Lattanzi and J. I. Silk, *Can the WIMP annihilation boost factor be boosted by the Sommerfeld enhancement?*, *Phys. Rev. D* **79** (2009) 083523, [0812.0360].